Designing, Spectral Confirmation, Hirshfeld Surface Analysis and Investigation of DNA Binding and Antibacterial Potentials as well as DFT, Molecular Docking and ADMET Evaluation of Hydrazide Based Schiff Bases

[1]Aiman Siddique, [2]Muhammad Sirajuddin*, [1]Ali Haider, [1]Saqib Ali**, [3]Muhammad Nawaz Tahir, [4]Moazzam Hussain Bhatti

[1]*Department of Chemistry, Quaid-i-Azam University, Islamabad, 45320, Pakistan.*
[2]*Department of Chemical Sciences, University of Science & Technology, Bannu, 28100, Pakistan.*
[3]*Department of Physics, University of Sargodha, Sargodha, Pakistan.*
[4]*Department of Chemistry, Allama Iqbal Open University Islamabad, Pakistan.*
m.siraj09@gmail.com*, saqibali@qau.edu.pk**

(Received on 27th January 2026, accepted in revised form 10th April 2026)

Summary: Two Schiff bases have been synthesized in three steps: first by reacting 2-(2,4-dichlorophenoxy)acetic acid with ethanol to give ethyl 2-(2,4-dichlorophenoxy)acetate, which was then treated with hydrazine to give 2-(2,4-dichlorophenoxy)acetohydrazide (**a**) in the 2nd step, and in the 3rd step, it was further reacted separately with salicylaldehyde and 4-(diethylamino)salicylaldehyde to give the final products (*E*)-2(2,4-dichlorophenoxy)-*N*′-(2-hydroxybenzylidine)acetohydrazide (**1**) and (*E*)-2-(2,4-dichlorophenoxy)-*N*′-(4-diethylamino)-2-hydroxybenzylidene)acetohydrazide (**2**). The products of each step were confirmed *via* instrumental techniques (FTIR, NMR and single crystal XRD). The crystal systems with space groups of **a** & **2** were triclinic & P-1 and monoclinic & P 21/n, respectively. The ADMET studies explored the potency of the screened compounds as drug. The compounds were tested for interaction with DNA using UV-Vis spectroscopy, viscosity measurement and molecular docking and results obtained from both studies suggest the intercalative mode of interaction. Both the compounds **1** & **2** have shown significant activity against the studied bacterial strains as compared to the standard drug Ciprofloxacin. The ADMET properties of compounds **1** & **2** were examined with the help of ADMETLab 3.0 to determine their drug-like characteristics. The drug-likeness and drug score of compounds **1** & **2** are 5.86 & 0.09 and 6.4 & 0.07, respectively. DFT study shows that the compounds have good chemical reactivity due to small energy gap value (ΔE). The red lines in the contour map are due to the presence of strong electron withdrawing oxygen atoms.

Keywords: Schiff base, Crystal structure, DFT, ADMET study, Docking study, HAS.

Introduction

In 1864 German Scientist Hugo Schiff prepared the organic compound containing (>C=N-) moiety. These are also known as azomethine or imine moieties [1-3]. In these compound the C=N moiety plays a substantial part in biological activity due to the availabilty of the lone pairs of electrons in the sp^2 hybridized orbital of the methylene N atom [4]. They are found both in nature and prepared in the laboratory [5]. Among Schiff base derivatives such as hydrazies, dihydrazies, hydrazones and mixed derivatives (hydrazide-hydrazones) [5-7] we have chosen the hydrazine based type because of both biological and non-biological applications such as catalytic role in asymmetric aldol reaction, [8] as substrate in regioselective reactions for azohetrocycles preparation, [9] in cyclization of hydroamination and aminocarbonylation, [10] as sulfenylating reagents in reaction used to obtained indole thioethers [11].

Schiff bases have attracted considerable attention in medicinal and coordination chemistry due to their structural diversity, facile synthesis, and diverse biological activities. The azomethine functional group plays and important role in coordination, electron delocalization, biological interactions. Owing to their tunable electronic and steric properties, Schiff bases and their derivatives have been widely investigated for different biological activities. Recent studies have demonstrated that hydrazide-based Schiff bases and their metal complexes have shown significant biological potential, partly due to their ability to interact with biomolecules such as DNA and proteins, making them

***To whom all correspondence should be addressed.**

promising scaffolds for drug development and medicinal applications [12, 13].

Hydrazides are a vital class of compounds with biological activity. The hydrazides and their condensation products has numerous biological applications, including antifungal, antibacterial, tuberculostatic, HIV inhibitory, and pesticidal effects. Certain hydrazides and corresponding hydrazones are psychopharmacological agents, including serotonin antagonists and monoamine oxidase (MAO) inhibitors. In addition to being intermediates, hydrazide-hydrazone compounds are also highly potent chemical substances on their own. The active hydrogen component of the -CONHN=CH-azomethine group can be used to produce novel derivatives when they are employed as intermediates [14].

Schiff base ligands with hydrazide moiety are known as "privileged ligands" because they are used widely not due to their solubility in common organic solvents but also easiest synthetic procedure and innovative structural motifs [15]. Due to the enormous applications in medicinal chemistry and flexible properties of the hydrazine based Schiff bases made them as a prominent class of organic compounds [16, 17].They reported with multiple therapeutic contexts including anti-oxidant, [18] anti-bacterial, [19] anti-fungal [2], anti-glycating [20], anti-diabatic [21], anti-inflammatory [22], ureas, prolyl oligopeptidase [23] α- amylase and tryosinase inhibitory potentials [24].In addition to medicinal applications, hydrazone-Schiff bases derivatives also act as effective metal ion chelator (chelation therapy) for metal overload diseases. Importantly, they play vital roles in designing and developing of drug because of their diversity in structures as well as their relative ease of synthesis and ability to modifymolecular properties. The hydrazone-Schiff bases are significantly impactful in medicinal chemistry because they can improve therapeutic strategies by means of targeted and focused drug design, alongside versatile applications.

The process of developing new drugs is a prolonged one that involves significant risk, expensive expenditures, and high attrition rates. In addition to laying the essential foundation, the preclinical stage is a challenging stage of drug development that faces a significant attrition rate of over 93% [25, 26]. More than 75% of drugs proposals get fail during clinical trials and drug approval procedure, even if some make it to clinical research [27, 28]. About 40% of candidate molecules fail in this procedure due to undesired pharmacokinetic characteristics, such as ADME qualities. Rendering to them, up to 30% of drug development failures can also be attributed to toxicity, another crucial evaluation metric. This emphasizes how ADME and toxicity (ADMET) features have a significant influence on whether drug development efforts are successful overall and how crucial it is to evaluate ADMET properties early on [29].

Here in this study we have prepared organic donor compounds containing hydrazine [-N-NH-C=O], Schiff base moiety [-CH=N-]and phenolic [OH] donor functionalities (O, N, O-donor set) linked with salicylaldehyde and 4-(diethylamino) salicylaldehyde, respectively. The ADMET properties of these synthesized compounds were evaluated. A DFT study was carried out to get the theoretical understanding of the electronic structure (HOMO-LUMO, energy gap, stability and related reactivity parameters) while and molecular docking study was performed in order to know the possible binding interactions between the studied compounds and the target protein.

Experimental

Materials and methods

The synthetic work involved the use of highly pure chemicals. Salicylaldehyde, 4-(diethylamino) salicylaldehyde, sulphuric acid, $NaHCO_3$, 4-dichlorophenoxy acetic acid were utilized without further purification after being purchased from Aldrich. The melting point was determined using capillary tubes with the help of MPD Mitamura Riken Kogyo apparatus. FTIR spectra between 4000 and 450 cm^{-1} were recorded while NMR spectra were measured in DMSO. The UV-Vis 1800 Shimadzu spectrophotometer was used to detect absorption. A Bruker Smart Apex Diffractometer was used to get the crystal data.

*Synthesis of 2-(2,4-dichlorophenoxy)acetohydrazide (**a**) using ethyl 2-(2,4-dichlorophenoxy)acetate*

The compound **a** was prepared by dissolving 2,4-dichlorophenoxy acetic acid (6 mM) in ethanol (50 mL) and concentrated H_2SO_4 (3 mL) added slowly in a two necked flask (Scheme 1). The mixture was refluxed for 8 hours. The brownish yellow oily product was obtained, cooled and purified by solvent extraction method using ethyl ester (20 mL), ethyl acetate (30 mL) and $NaHCO_3$ (20 mL). After well shaking, two layers were separated and the final product was obtained after rotary evaporation of the solvent. Ethyl 2-(2,4-dichlorophenoxy)acetate (5 mM) in ethanol (50mL) was reacted hydrazine hydrate (25 mL) by refluxing for 15 hours. A white shiny crystal product obtained in good yield (90%) which was filtered and finally washed with ethanol. The melting point of **a** was determined and found 161-163°C.

Elemental Analysis (Theoretical/Experimental): C, 40.88 (40.81); H, 3.43 (3.40); N, 11.92 (11.98).

FTIR ν (cm^{-1}): 3500-3300 (broad peak for NH, NH_2), 1667 (C=O), 1245 (C-O), 836 (C-Cl).

NMR (DMSO, δ, ppm): ^{1}H**:** 9.29 (s, 1H, NH), 7.55 (1H, H7, d, ^3J = 2.7 Hz), 7.35 (1H, H5, dd, ^3J= 2.7 Hz), 7.06 (1H, H4, d, ^3J = 9 Hz), 4.58 (s, 2H, H2), 3.70 (s, 2H, NH_2).

^{13}C: 166.6 (C1); 152.9 (C3),129.8 (C7), 128.5 (C5), 125.6 (C6), 123.0 (C8), 115.6 (C4), 67.4 (C2).

Synthesis of Compound **1**

The compound **1** was synthesized by dissolving (0.7 g) of (**a)**into 50 mL of THF and (0.31 mL) of salicylaldehyde using 1:1 molar ratio and system was refluxed for 4 hours to get the white solid product which was washed with THF to remove if any unreacted 2-(2,4-dichlorophenoxy)acetohydrazide is there. The melting point of the desired compound **1** was 186-189°C and yield of 85%.

Elemental Analysis (Theoretical/Experimental): C, 53.12 (53.51); H, 3.57 (3.60); N, 8.26 (8.28).

FTIR ν (cm^{-1}): 3420 (OH), 3320 (NH), 1738 (C=O), 1673 (N=CH), 1289 (C-O), 763 (C-Cl).

NMR (DMSO, δ, ppm):^{1}H: 11.87 (s, 1H, OH), 10.04 (,1H, NH), 8.31 (s, 1H, H7), 7.73 (d, 1H, H5, ^3J = 7.7 Hz), 7.53 (s, 1H, H14), 7.25 (t, 1H, H3, ^3J = 6.9 Hz), 7.14 (d, 1H, H12, ^3J = 8.9 Hz), 7.09 (d, 1H, H11, ^3J = 8.9 Hz), 6.91 (t, 1H, H4, ^3J = 7.5 Hz), 6.85 (d, 1H, H2, ^3J = 7.5 Hz), 4.83 (s, 2H, H9).

^{13}C:168.4 (C8); 157.7 (C1),153.3 (C10), 148.3 (C7), 131.7 (C3), 130.0 (C14), 129.7 (C5), 128.3 (C12), 126.8 (C13), 124.9 (C15), 120.5 (C4), 116.8 (C2), 115.9 (C6), 115.6 (C11), 67.8 (C9).

Synthesis of Compound **2**

The compound **2** was synthesized by dissolving (0.7 g) of (**a)** into 50 mL of THF and (0.57 g) of 4-(diethylamino) salicylaldehyde using equimolar ratio. The mixture was refluxed for 3.5 hours. The light-yellow fluffy product was obtained after refluxing the mixture for 3.5 hours followed by rotary evaporation of solvent. The melting point of the desired product was 192-194°C and yield of 83%.

Elemental Analysis (Theoretical/Experimental): C, 55.62 (55.51); H, 5.16 (5.20); N, 10.24 (10.32).

FTIR ν (cm^{-1}): 3404 (OH), 3315 (NH), 1730 (C=O), 1628 (N=CH), 1291 (C-O), 760 (C-Cl).

NMR (DMSO,δ, ppm):^{1}H:11.13 (s, 1H, OH), 9.78 (s,1H, NH), 8.26 (s, 1H, H9), 7.62 (d, 1H, H16, ^3J = 2.5 Hz), 7.40 (d, 1H, H7, ^3J = 8.9 Hz), 7.21 (d, 1H, H14, ^3J = 8.8 Hz), 7.06 (d, 1H, H13, ^3J = 8.9 Hz), 6.24 (dd, 1H, H8, ^3J = 2.2 Hz), 6.11 (d, 1H, H4, ^3J = 2.5 Hz), 4.78 (s, 2H, H11), 3.38 (q, 3H, H1, ^3J = 8.6 Hz), 1.10 (t, 2H, H2, ^3J = 7 Hz).

^{13}C: 167.5 (C10); 158.7 (C5), 153.3 (C12), 150.7 (C3), 144.3 (C9), 131.9 (C7), 129.9 (C16), 128.5 (C14), 125.6 (C15), 123.0 (C17), 115.9 (C13), 104.4 (C6), 104.2 (C8), 97.8 (C4), 67.6 (C11), 44.2 (C1), 13.0 (C2).

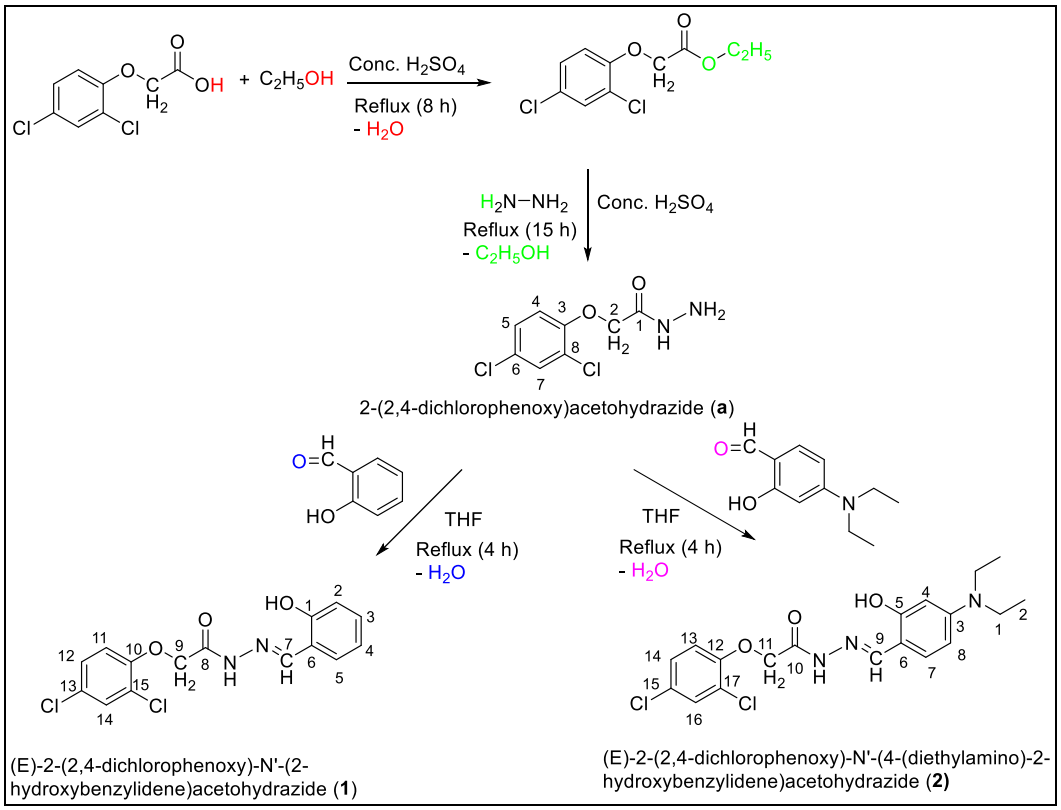

Scheme-1: Systematic view of the synthesized compounds along with NMR numbering pattern

Compounds-DNA Interaction Study by UV-Vis. Spectroscopy

The compounds (**1** and **2)** interaction with SS-DNA was studied using UV-Vis. absorption spectroscopy. First the SS-DNA purity was checked using the absorbance ratio (260/280) and was found 1.9 indicating free of protein. The absorbance of 1 mM solutions of compounds **1** and **2** was measured and to them separately known conc. of DNA was added and the mixtures were left for 10 minutes. After that their absorbance were measured. The same conc. of DNA was added to the blank solutions to avoid the effect of DNA itself. The binding constant was found from the ratio of slop-to-intercept of the plot of $A_o/A\text{-}A_o$ *vs.* 1/[DNA] [30, 31].

Compounds-DNA Interaction Study by Viscosity Measurement

The compound-DNA interaction was also carried out by viscosity measurement following the protocol reported by Murtaza et. al [32]. The viscosity was measured using an Ubbelodhe viscometer at room temperature. Three simultaneous readings of the flow time were taken using a digital stopwatch, from which the average flow time was calculated. The results were presented as $(\eta/\ \eta_o)^{1/3}$ *vs.* binding ratio (r) of [Compound]/[DNA], where η is the relative viscosity of DNA in the presence of test compounds and ηo is the relative viscosity of DNA itself.

Confirmation of Compound-DNA study by Molecular Docking Study

The mechanism of interaction of the compounds with the DNA was further studied using the MOE dock software V-2015. From the protein data library, the 3D structure of DNA with PDB# 1BNA was acquired. Five conformations were made for every ligand. For additional study of molecular interactions, the conformation of each compound with minimum binding energy was used for docking [33].

Antibacterial Activity

Both the compounds **1** and **2** were tested against the following bacterial strains including *E. coli*, MRSA, MSSA, *E. faecalis*, *P. aeruginosa* using disc diffusion method. The zones of inhibition were calculated in millimeters and performing the experiment in triplicate. Ciprofloxacin (5µg/disc) was used as reference drug [30].

In Silico ADMET Evaluation

ADMETlab 3.0, which is publically available at https://admetlab3.scbdd.com without registration, was used to conduct the in silico investigation. The website immediately displays the results, which can be downloaded in optional forms. The information was entered using SMILES that were taken from ChemBiodraw Ultra 14.

Density Functional Theory (DFT) Study

The DFT study was carried using Gaussian 09 program with B3LYP level and 6-31G'++ (d, p) basis set in order to get the optimized gaseous phase geometries. Gauss view 5.0 program was used for input data files and visualization of results [34].

Hirshfeld surface Analysis (HSA)

The software CrystalExplorer 17.5 was used to create 2D fingerprint plots and analyze the Hirshfeld surface in which the molecules within the crystals are bind together by intermolecular forces [35]. HSA plots the d_{norm}, shape index, curvedness, and electrostatic potential to reveal the interactions. Using the colors red, white, and blue, the interactions within the crystal were seen on the Hirshfeld surface [36]. CrystalExplorer17.5 was used to compute the energy frameworks and interaction energies between molecule pairs [37].

Results and Discussion

FT-IR description

The formation of Ethyl 2-(2,4-dichlorophenoxy)acetate (**a**) was confirmed by the esterification of 2,2-dchlorophenoxyacetic acid giving a prominent ester peak (C-O-C) peak at 1201 cm^{-1}. This product (**a**) was then converted into 2-(2,4-dichlorophenoxy)acetohydrazide (**b**) giving a broad peak for NH and NH_2 in the range of 3500-3300 cm^{-1}. The Schiff bases **1** and **2** were confirmed by the presence of imine peaks (-N=CH) at 1673 cm^{-1} and 1628 cm^{-1}, respectively.

NMR description

The compounds **1** and **2** were confirmed by the presence of the imine proton (-N=CH) at 8.309 ppm (H7 in **1**) and 8.26 ppm (H9 in **2**). Similarly, in the ^{13}C NMR spectra resonance for this imine carbon was observed at 148.3 ppm (C7 in **1**) 144.3 ppm (C9 in **2**). The OH and NH signals in **1** and **2** appeared at 11.876 ppm & 11.135 ppm and 10.043 ppm & 9.779 ppm, respectively.

Crystals description

The molecule (**a**) crystallizes in a triclinic system with space group P-1 and the empirical formula $C_8H_8N_2O_2Cl_2$ (M = 235.06 g/mol). Throughout the data gathering process, the crystal was maintained at 296(2) K. The cell parameters are as follows: α = 94.794(5)°, β = 90.031(4)°, γ = 98.548(5)°, a = 7.3444(14) Å, b = 8.1170(15) Å, and c = 8.5289(14) Å. The resulting wR_2 was 0.1051 (all data) and R_1 was 0.0374 ($I > 2\sigma(I)$). Figs 1 and 2 depict the crystal structure and packing diagram of a, and Table S1 in the supplemental material provides information on the crystal properties. Tables 1 and 2 list the chosen bond lengths and angles. One molecule makes up the asymmetric unit of a. Non-covalent H-bonding interactions N-H–O and C-H–Cl stabilize the packing of a (Fig 1B).

Table-1: Bond lengths for **a** & **2.**

A								
Atoms		**Length/Å**	**Atoms**		**Length/Å**	**Atoms**		**Length/Å**
Cl1	**C2**	**1.7338(15)**	**C1**	**C2**	**1.393(2)**	**N1**	**N2**	**1.411(2)**
Cl2	**C4**	**1.7424(17)**	**C1**	**C6**	**1.392(2)**	**N1**	**C8**	**1.330(2)**
O1	**C1**	**1.3567(19)**	**C2**	**C3**	**1.374(2)**	**C5**	**C6**	**1.378(3)**
O1	**C7**	**1.4254(19)**	**C3**	**C4**	**1.378(2)**	**C7**	**C8**	**1.503(2)**
2								
Cl1	**C1**	**1.733(3)**	**N3**	**C13**	**1.371(5)**	**C7**	**C8**	**1.501(4)**
Cl2	**C4**	**1.735(3)**	**N3**	**C16A**	**1.458(10)**	**C9**	**C10**	**1.438(5)**
O1	**C16**	**1.360(4)**	**N3**	**C18A**	**1.455(10)**	**C10**	**C11**	**1.394(5)**
O1	**C7**	**1.423(4)**	**C16**	**C1**	**1.381(5)**	**C10**	**C15**	**1.391(5)**
O2	**C8**	**1.213(4)**	**C16**	**C6**	**1.384(4)**	**C11**	**C12**	**1.372(5)**
O3	**C11**	**1.349(4)**	**C1**	**C3**	**1.378(5)**	**C12**	**C13**	**1.397(5)**
N1	**N2**	**1.376(4)**	**C3**	**C4**	**1.373(5)**	**C13**	**C14**	**1.390(6)**
N1	**C8**	**1.340(4)**	**C4**	**C5**	**1.367(5)**	**C14**	**C15**	**1.359(5)**
N2	**C9**	**1.276(4)**	**C5**	**C6**	**1.383(5)**	**C16A**	**C17A**	**1.509(10)**

The molecule **2** with an empirical formula $C_{19}H_{21}Cl_2N_3O_3$ (*M* =410.29 g/mol) crystalizes in monoclinic system with space group $P2_1/n$. The crystal was also kept at 296(2) K during data collection. The cell parameters for **2** are: *a* = 4.9821(5) Å, *b* = 13.4582(15) Å, *c* = 29.521(3) Å, *β* = 91.201(6)°. The final R_1 was 0.0723 ($I > 2\sigma(I)$) and wR_2 was 0.1689 (all data). The crystal structure and packing diagram of **2** are shown in Figs 1 &2. In compound **2**, the 2,4-dichlorophenoxy part A (C1-C6, O1, Cl1, Cl2), acetohydrazide part B (C7, C8, N1, N2, O2) and the part of [4-(diethylamino)-2-hydroxyphenyl]methylidene C(C9-C15/N3) are planar having r. m. s. deviation of 0.0121, 0.0053 and 0.0279 Å, respectively. The diethyl parts are disordered over two orientations having occupancy ratio of 0.901(6): 0.099(6). The H-atom of OH group from a strong intramolecular O–H···N hydrogen bond. Two different types of strong intramolecular H-bonding are observed as shown in Fig 2A: N1-H1-O1 with d(H-A) of2.46 Å and N2-H2-Cl2 with d(H-A) of2.21(3) Å. Another types of weak H-bonding also exist whose detail is given in Table 3. Molecules linked in a zig-zag array along the b-axis were observed in the packing diagram of **2** (Fig 2). The

molecules are interconnected in form of dimers due to intermolecular H-bonding's of C-H…O type to complete $R_2^2(8)$ and $R_2^1(7)$ rings Fig3. The intramolecular N-H…O and O-H…N type interactions ample S(5) and S(6) members ring motifs S(5) and S(6) ring motifs. The dimers are further connected to each other due to C-H…Cl bonding.

Table-2: Bond angles for **a** and **2.**

A											
Atoms			Angle/°	Atoms			Angle/°	Atoms			Angle/°
C1	O1	C7	117.42(12)	C3	C4	Cl2	118.48(14)	C3	C2	Cl1	119.23(13)
C8	N1	N2	122.75(14)	C3	C4	C5	120.87(16)	C3	C2	C1	121.58(14)
O1	C1	C2	116.21(13)	C5	C4	Cl2	120.64(13)	C2	C3	C4	118.97(16)
O1	C1	C6	125.57(14)	C6	C5	C4	119.80(15)	O2	C8	N1	123.62(16)
C6	C1	C2	118.22(15)	C5	C6	C1	120.56(16)	O2	C8	C7	118.39(15)
C1	C2	Cl1	119.19(12)	O1	C7	C8	110.26(13)	N1	C8	C7	117.99(14)
2											
C16	O1	Cl7	118.3(3)	O2	C8	N1	124.5(3)	C3	C1	Cl1	119.6(3)
C8	N1	N2	120.8(3)	O2	C8	C7	119.9(3)	C3	C1	C16	121.4(3)
C9	N2	N1	116.1(3)	N1	C8	C7	115.6(3)	C4	C3	C1	118.8(3)
C13	N3	C16A	102(2)	N2	C9	C10	122.9(4)	C3	C4	Cl2	119.1(3)
C13	N3	C18A	106(2)	C11	C10	C9	123.1(3)	C5	C4	Cl2	119.9(3)
C18A	N3	C16A	134(4)	C15	C10	C9	121.1(4)	C5	C4	C3	121.1(3)
O1	C16	C1	116.8(3)	C15	C10	C11	115.8(3)	C4	C5	C6	119.9(3)
O1	C16	C6	124.5(3)	O3	C11	C10	121.2(3)	C5	C6	C16	120.2(3)
C1	C16	C6	118.7(3)	O3	C11	C12	117.8(4)	O1	C7	C8	110.0(3)

Table-3: Hydrogen bonding for **a** & **2.**

a						
D	H	A	d(D-H)/Å	d(H-A)/Å	D(D-A)/Å	D-H-A/°
N1	H1	$N2^1$	0.86	2.46	3.102(2)	131.9
N2	H2A	$Cl2^2$	0.85(3)	2.86(3)	3.657(2)	156(2)
N2	H2B	$O2^3$	0.88(3)	2.21(3)	3.083(2)	171(2)
C3	H3	$Cl1^4$	0.93	2.95	3.8117(19)	154.3
C5	H5	$Cl2^5$	0.93	2.89	3.7727(18)	159.3
C6	H6	$O2^6$	0.93	2.47	3.361(2)	159.9
2						
O3	H3A	N2	0.82	1.93	2.656(4)	146.7
C6	H6	$O2^1$	0.93	2.59	3.383(4)	143.2
C7	H7B	$O2^1$	0.97	2.58	3.485(4)	155.8
C17A	H17A	$O3^2$	0.96	2.60	3.37(5)	137.6
C19A	H19C	$Cl2^3$	0.96	2.80	3.69(5)	154.7
O3	H3A	N2	0.82	1.93	2.656(4)	146.7

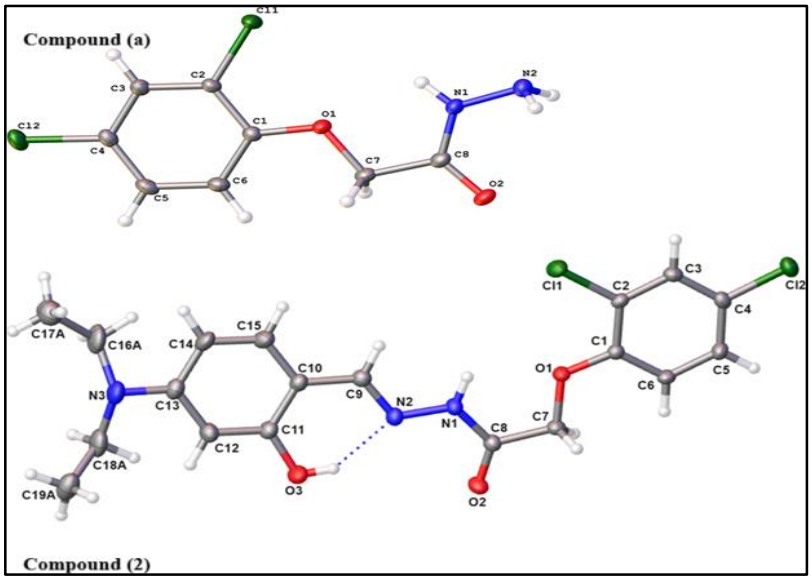

Fig 1. ORTEP view of **a** and **2**.

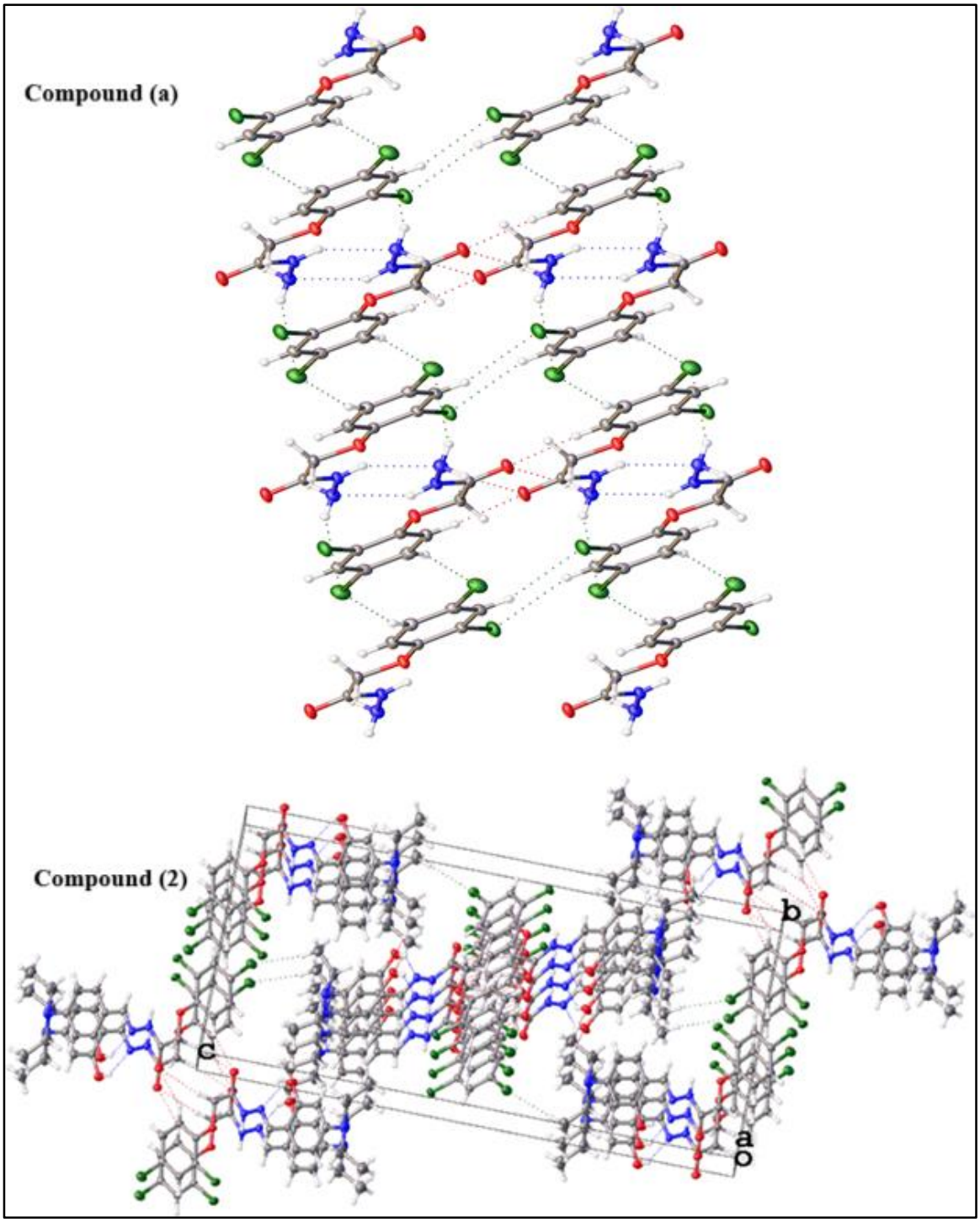

Fig. 2: Packing diagram of a and 2 with inter-/intramolecular H-bonding shown by dotted lines.

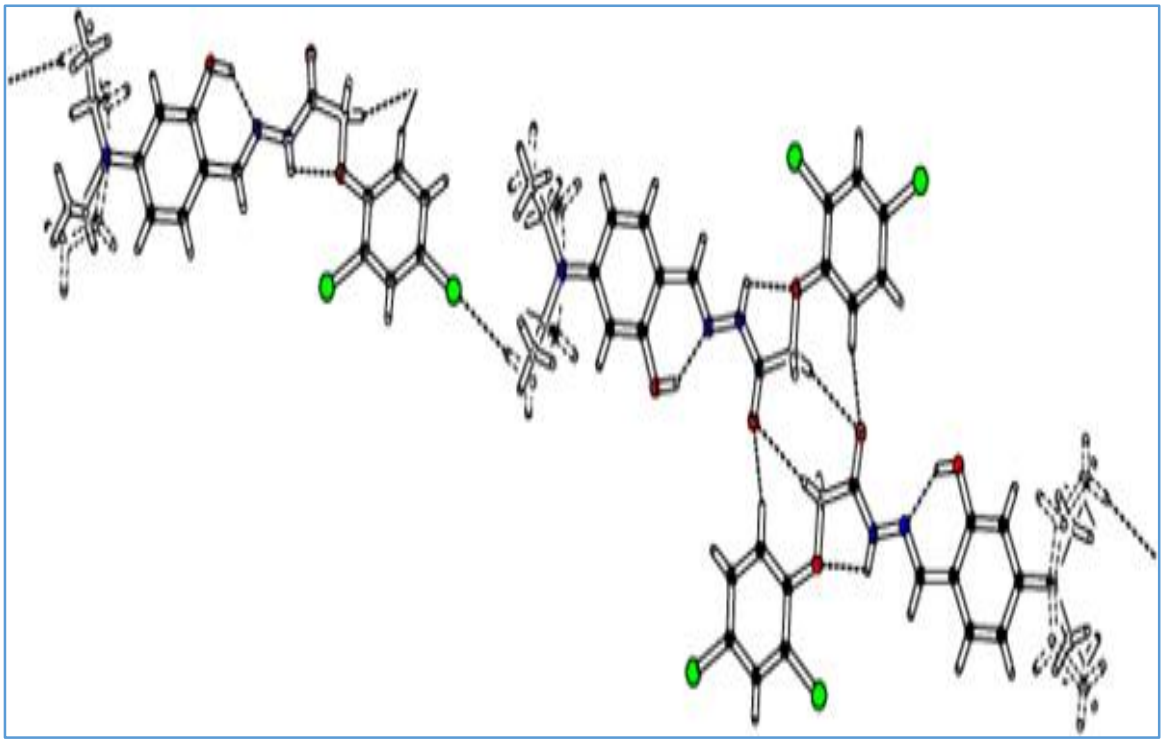

Fig. 3: Formation of $R_2^2(8)$ and $R_2^1(7)$ rings in the form of dimers. Intramolecular N-H…O and O-H…N type of bonding completes S(5) and S(6) ring motifs.

UV-Vis. Spectroscopy for Compound-DNA Binding Study

UV-Vis. spectroscopy was employed to know about the binding nature of the compounds with DNA. The Figs 4A and B represent the binding of compounds **1** and **2** with SS-DNA, respectively. Both the compounds experiences hypochromic shift along with red shift (~ 3 nm) upon the addition of increasing concentration of SS-DNA. These two phenomenon are sign of interaction mode of interaction. The binding constant (K_b) for the compound-DNA adduct was found form inside graph (b) using the intercept to slop ratio and were found to be 1.5 x 10^4& 1.96 x 10^4 M^{-1}, respectively for compounds **1** and **2**.Similarly, their ΔG values are -24.0 & -24.49 kJ/mol and negative sign indicate the spontaneity of the compound-DNA adduct formation [38, 39].

Viscosity Measurement for Compound-DNA Binding Study

Viscosity measurements were performed to further understand the method of binding of compounds to DNA. The increase in DNA viscosity caused by base pair dissociation to lodge the binding compound is best explained by the traditional intercalation hypothesis. A discernible rise in DNA's viscosity with the addition of the test compound, which causes the DNA base pairs to separate, is indicative of the intercalation effect [32]. When compounds 1-2 were added to the DNA solution, the relative viscosity increased, which was indicative of the compounds' primarily intercalating binding nature. The plot of $(\eta/\eta_o)^{1/3}$ vs. [Compound]/[DNA] provides a measure of the viscosity changes (Fig 5) that occurred due to intercalation.

Compound-DNA interaction by Molecular Docking

The compound-DNA interaction was also confirmed theoretically by molecular docking using MOE software. The intercalative interaction between the DNA and compounds (**1** & **2**) is shown in Figs 5A&B. The docking scores of compounds **1** and **2** are -7.39 and -7.59 while their rmsd are 3.23 and 2.15 Å, respectively. Compound **1** interact with DT A8 nucleotide of DNA in H-acceptor fashion with binding energy of 3.38 kcal/mol and distance of -1.2Å (Fig 6A) while compound **2** interacts with DG A10 nucleotide in H-donor fashion *via* NH and CH_2 groups with binding energies of 3.62, 3.52 kcal/mol and distances of -0.83, -0.6Å, respectively (Fig 6B).

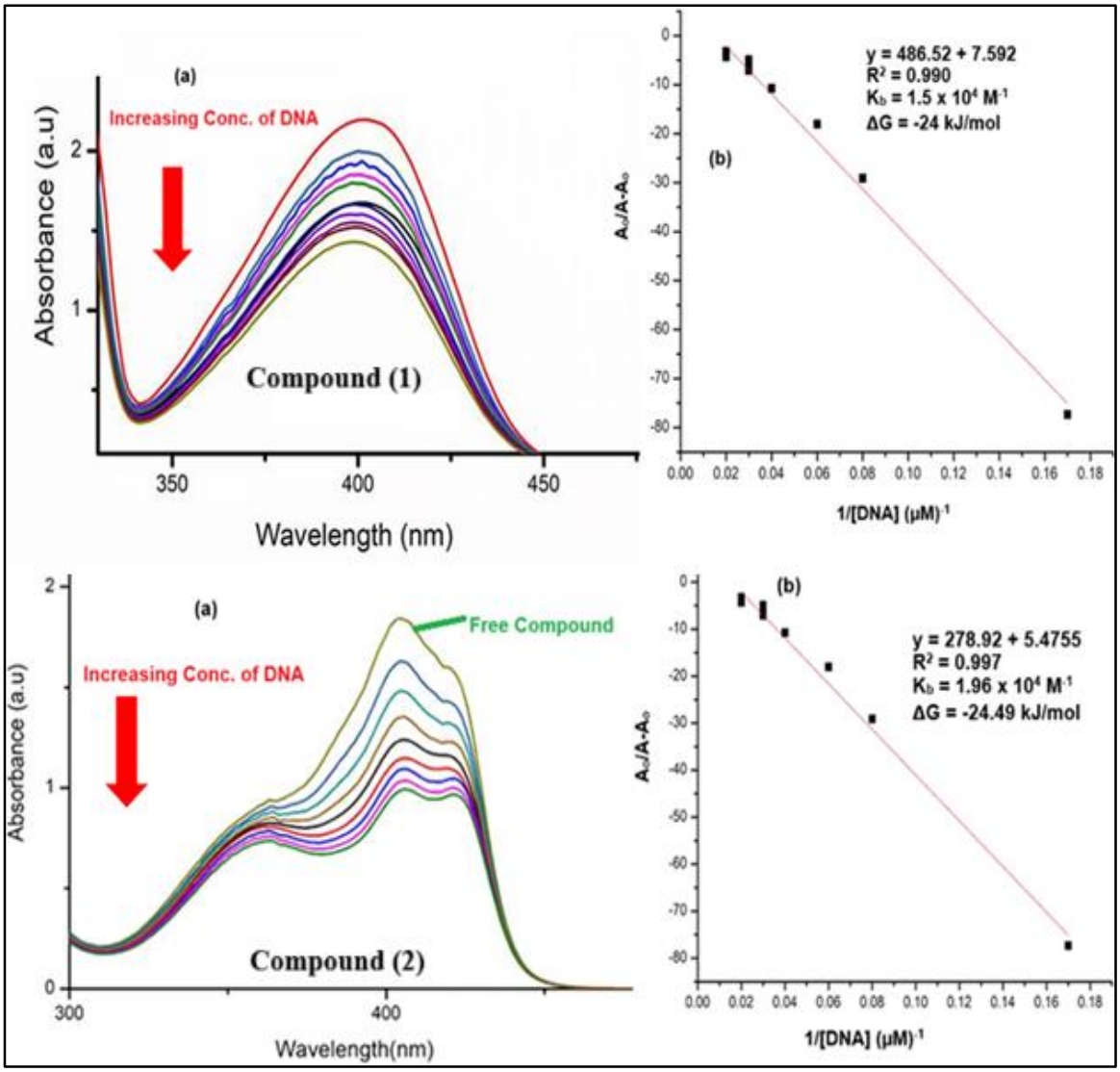

Fig. 4: Interaction of compounds **1** & **2** with SS-DNA.

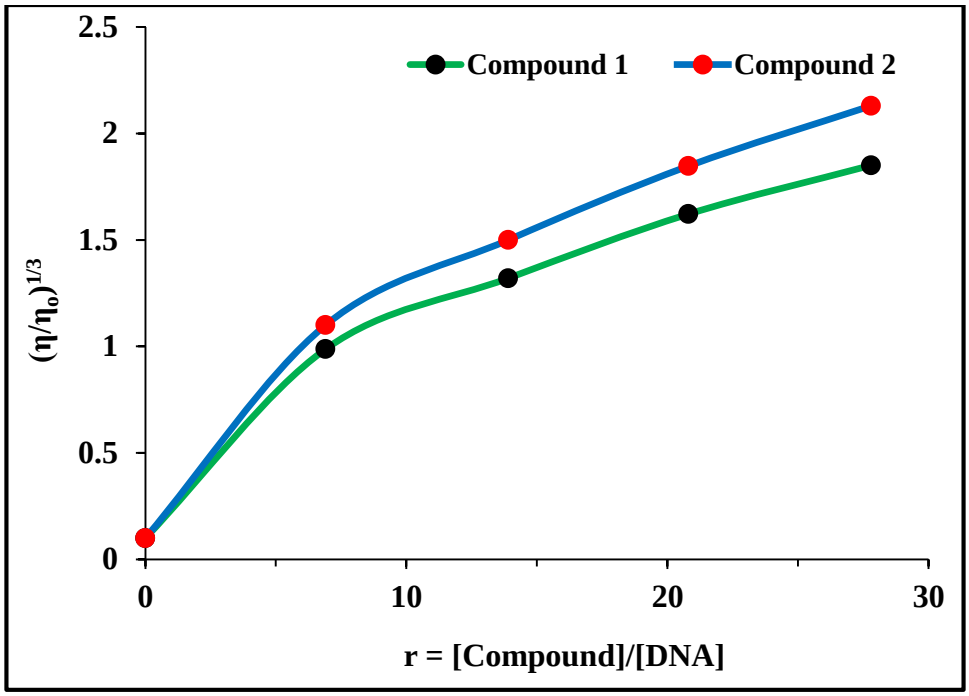

Fig. 5: Plot of relative viscosity of SS-DNA at different binding ratio (r) of the compounds (1 & 2).

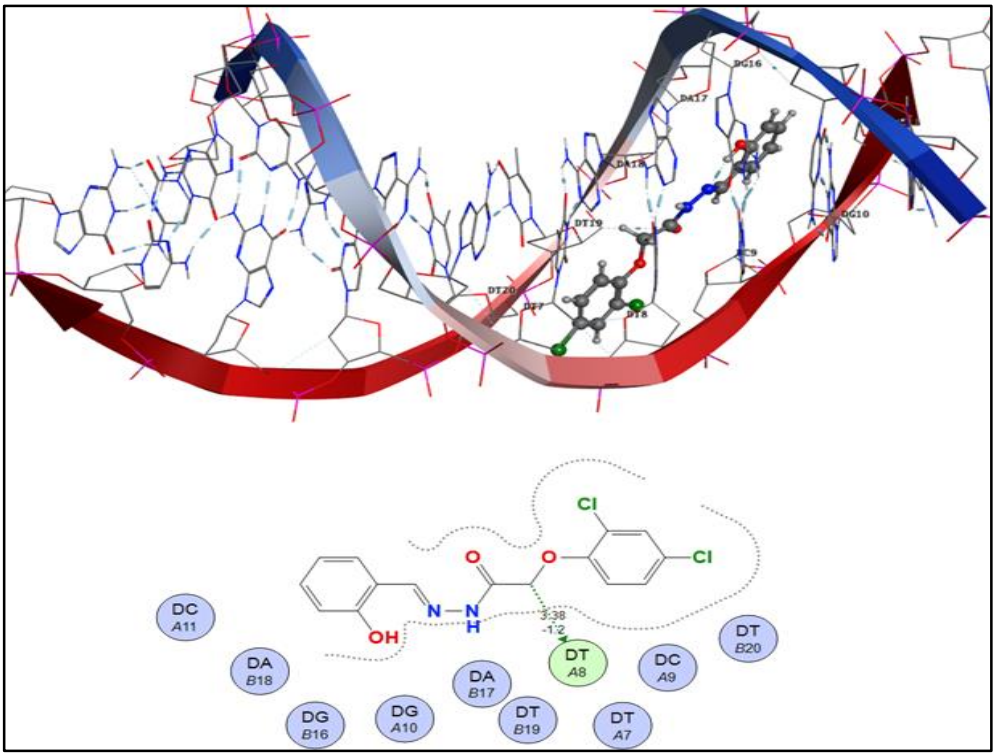

Fig. 6A: Intercalative docking view of compound 1 with DNA along with 2D view of interaction

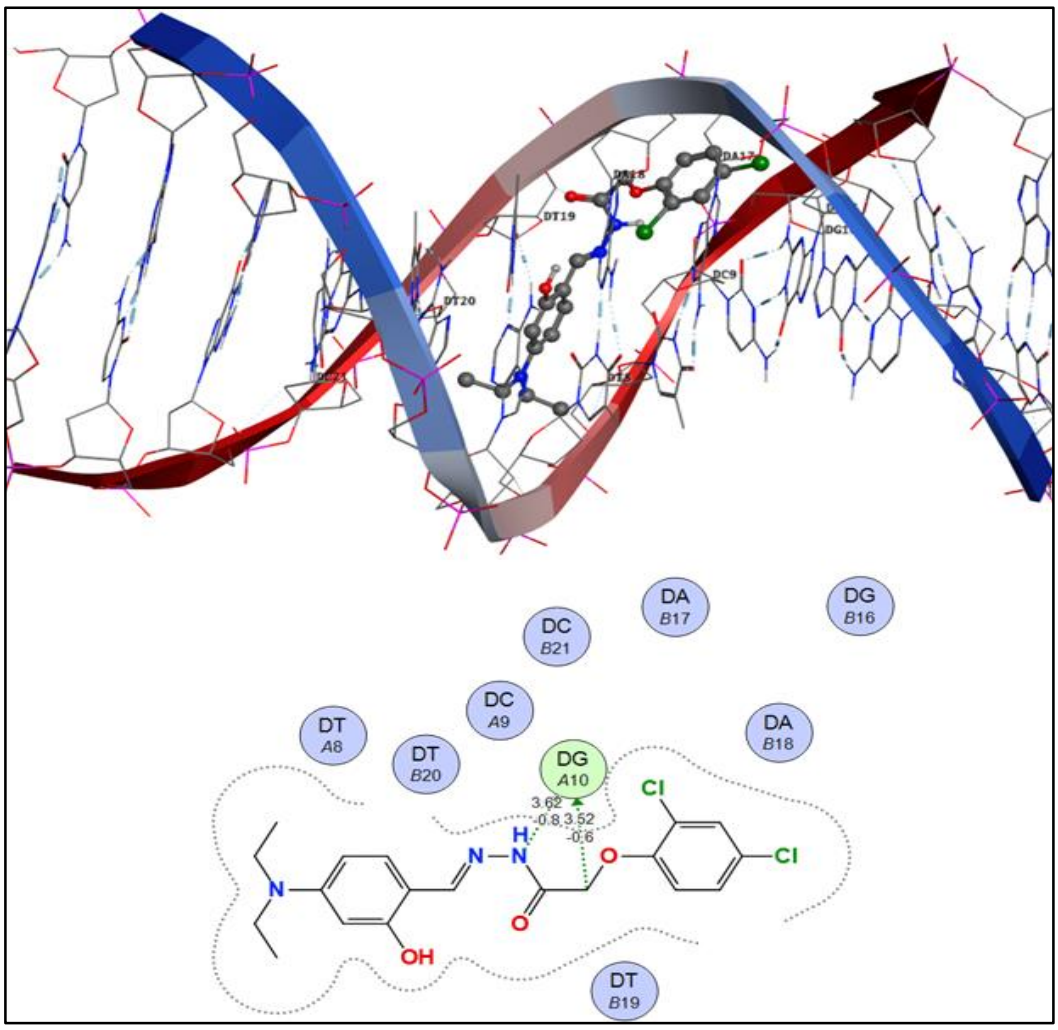

Fig. 6B: Intercalative docking view of compound 2 with DNA along with 2D view of interaction.

Antibacterial Results

The antibacterial screening results of compounds 1 and 3 against the tested bacterial strains are given in Table 4. A compound is said to have significant activity if its zone of inhibition > 20 mm. if the zone of inhibition is in the range of 18-20 mm then activity is good and if in the range of 15-17 mm then low and if < 11-14 mm then non-significant [2]. The data in Table 5 indicates that the activity of the both the compounds **1** and **2** possess significant activity against the tested bacterial strains.

Table-4: Antibacterial activity data of compounds **1**&**2.**

Comp. #	Zone of Inhibition (mm)					
	K. pneumonia	*E. coli*	MRSA	MSSA	*P. aeruginosa*	*E. faecalis*
1	**21**	**21**	**26**	**28**	**21**	**28**
2	**22**	**22**	**26**	**28**	**26**	**28**
Ciprofloxacin	**24**	**28**	**18**	**25**	**25**	**24**

ADMET description

According to the drug-like soft rule, the evaluated compounds' physicochemical characteristics fell within the drug-recommended range. The Veber rule's allowed the drug range is met by both compounds' TPSA (Fig 7) as it plays a crucial role in the discovery of drugs because low solubility hinders adequate and thorough oral absorption. The drug's suggested range for the logarithm of aqueous solubility value (logS) is -4 to 0.5 mol.L^{-1}. For the drug's approved range, the expected logP and logD7.4should be in between 0 and 3 log mol/L [40].The calculated values logS, logP, and logD7.4 values for **1** & **2** (Fig 7) differ only little from the maximum drug-recommended range seen in Radar view (Fig 8).

The drug-likeness and drug score were determined using the online webserver Molecular Properties Prediction - Osiris Property Explorer. The

+ve and –ve values of the tested compounds are used to analyze the drug-likeness model score; if the score is positive, the compound is comparable to a drug. Conversely, the compound is not a drug if the drug-likeness score is negative [41].The drug-likeness and drug score of compounds **1** and **2** is 5.86 & 0.09 and 6.4 & 0.07, respectively. The physicochemical data indicate the both the compounds **1** and **2** follow the Lipinski, Ghose and Veber rules of drug [42-44].

Absorption

How a medicine moves from the point of administration to the site of action is measured by absorption. One important measure of a drug's effectiveness is its bioavailability, which represents its percentage in the bloodstream. One of the most crucial steps in determining oral bioavailability is screening for absorption capacity. Therefore, to a certain degree, a compound's permeability value may serve as a significant indicator of its intestine absorption in humans. The most widely used methods for estimating in vivo drug permeability are PAMPA, MDCK, and Caco-2. A compound's expected Caco-2 permeability is as follows: If the anticipated value is > -5.15 log cm/s, the chemical is said to have high Cao-2 permeability; if not, it is deemed poor. The MDCK permeability prediction is as follows: When a compound's anticipated value is > 20 x 10-6 cm/s, it is said to have exceptional MDCK permeability; when it is between 2 and 20 x 10-6 cm/s, it is said to have medium permeability; and when it is < 2 x 10-6 cm/s, it is said to have low or poor permeability. The PAMPA technique mimics the gastrointestinal tract's passive diffusion absorption of medications taken orally. The limitations of individual models can be addressed by taking into account PAMPA in combination with the Caco-2 and MDCK models. This allows for a more precise prediction of a drug's absorption and penetration properties in the body. Low-permeability compounds were defined as having a log Peff value < 2.0, and high-permeability compounds were defined as having a log Peff value > 2.5. Excellent Caco-2, MDCK, and PAMPA permeability were demonstrated by the data collected for both compounds **1**&**2** (Fig 7).

If a compound's Pgp-inhibitor/substrate value falls between 0 and 1, it is considered an inhibitor or substrate; if it is zero, it is considered a non-inhibitor or substrate. The observed data for the reported compounds indicate that they are the excellent inhibitor as well as act as a substrate.

The key requirement for an oral medication's apparent effectiveness is its human intestinal absorption (HIA). If a molecule's absorbance is less than 30%, it is deemed poorly absorbed. Consequently, molecules designated as HIA- had an HIA >30%, and compounds classed as HIA+ had an HIA <30%. According to the findings, both compounds exhibit exceptional absorption.

F20%, F30% and F50% shows the 20%, 30% and 50% bioavailability of the compound, respectively. F20%-, F30%- and F50%- molecules were defined as having a bioavailability of at least 20%, 30% and 50%, respectively whereas F20%+, F30%+ and F50%+ molecules had a bioavailability of less than 20%, 30% and 50%, respectively. The likelihood of being F20%, F30%, or 30% is the output value, and it should fall between 0 and 1 (0-0.3: great; 0.3-0.7: medium; 0.7-1.0: poor). The data shows that for compound **1**, F20% and F50% bioavailability fall in the poor range while F30% in excellent range. Similarly, for compound **2**, F20%, F30% and F50% bioavailability fall in the medium, excellent and poor range, respectively (Fig 7).

Distribution

Plasma protein binding (PPB): Drugs with a high PPB value may have a poor therapeutic index, and a compound is said to have an appropriate PPB if its anticipated value is less than 90%. For example, < 90% indicates outstanding; otherwise, poor. The PPB value for compounds **1** and **2** falls in the range poor or low therapeutic index (Fig 7).

Volume of distribution at steady state (VDss): It is a basic pharmacokinetic (PK) characteristic of medications that quantifies the efficiency of a drug's distribution throughout the body. L/kg is the unit of expected VDss. If a compound's anticipated VDss fall between 0.04 to 20 L/kg, it is deemed to have an appropriate VD. i.e., 0.04–20: great; otherwise: subpar. Compounds **1** and **2** have VDss values that are in the bad range. The VDss value for compounds **1** and **2** falls in the poor range.

Fraction unbound (Fu) in plasms: The majority of drugs in plasma will alternate between being bound to serum proteins and being unbound. The degree to which a medicine binds blood proteins may have an impact on its effectiveness since the more tightly bound the protein, the less effectively it can diffuse or pass through cellular membranes. Compounds with >20% = High Fu; 5-20% = Medium Fu; <5% = Low Fu, i.e., Excellent ≥ 5%; bad < 5%. The Fu value for compounds **1** and **2** falls in the poor range (Fig 7).

Blood–brain barrier (BBB) Penetration: Compounds with logBBB> -1 were classified as BBB+ (excellent: 0-0.3; medium: 0.3-0.7; poor: 0.7-1.0), while compounds with logBBB ≤ -1 were classified as BBB-. The BBB value for compounds **1** and **2** falls in the excellent range.

Organic anion transporting polypeptide 1B1 (OATP1B1) and 1B3 (OATP1B3): Two crucial hepatic uptake transporters are OATP1B1 and OATP1B3. Drug-drug interactions may result from inhibition of their normal functioning. If a compound's value falls between 0 and 1 (excellent: 0-0.3; medium: 0.3-0.7; poor: 0.7-1.0), it is considered an OATP1B1 and OATP1B3 inhibitor; if it falls between 0 and 1, it is considered non-inhibitor. The data indicates that both the compounds **1** and **2** act as excellent OATP1B1 inhibitor while in case of OATP1B3 compound **1** is poor inhibitor while **2** is excellent.

Breast cancer resistance protein (BCRP): Drug-drug interactions and multi-drug resistance (MDR) to anti-cancer medications are significantly influenced by BCRP, an ATP-binding cassette (ABC) efflux transporter. In the early stages of drug discovery, the prediction of BCRP inhibition might help assess possible drug resistance and drug–drug interactions. BCRP: 0 to 1 (0-0.3 for excellent; 03-0.7 for medium and 0.7-1.0 for poor) and non-inhibitor BCRP: 0 indicate that a substance is a BCRP inhibitor. The data indicates that both the compounds **1** and **2** act as excellent BCRP inhibitor.

Multidrug resistance protein 1 (MRP1): MRP1 is a member of the ATP-binding cassette (ABC) protein superfamily and is an essential transmembrane efflux transporter. Across organs and physiological barriers, MRP1 regulates the absorption and elimination of a broad range of endogenous and exogenous substrates, including different medications. Drug-drug interactions may result from inhibition of their normal functioning. The data indicates that both the compounds **1** and **2** act as excellent MRP1 inhibitor.

Bile salt export pump (BSEP): A common adverse drug reaction is drug-induced cholestasis, which is typically brought on by an unanticipated interaction with BSEP. The primary membrane transporter in charge of moving bile acids from hepatocytes into bile is called BSEP. The data indicates that both the compound**1** acts as excellent BSEP inhibitor while **2** as poor inhibitors.

Metabolism

CYP1A2, CYP3A4, CYP2C9, CYP2C19, CYP2D6, CYP2B6, CYP2C8 substrate: Drug metabolism calculates the length and strength of a drug's action by measuring how specific enzyme systems break it down. The data indicates that both the compounds act as inhibitor as well as substrate for these CYP1A2, CYP3A4, CYP2C9, CYP2C19, CYP2D6, CYP2B6, CYP2C8 major drug-metabolizing enzymes.

Human liver microsomal (HLM): One of the most widely used assays for evaluating drug clearance by the human liver, the most crucial organ for drug metabolism, is the HLM stability assay. Compound **1** fall in the range of poor while **2** in the range of excellent.

Excretion: Drug excretion is the process by which drugs are eliminated from the body through a variety of pathways, including as sweat, saliva, and urine.

Plasma clearance (CL_{plasma}): CL_{plasma} is the only pharmacokinetic parameter that regulates total drug exposure (for a given bioavailability) and enables the calculation of the dosage necessary to maintain an average steady-state plasma concentration. By scaling the drug elimination rate (amount per time) by the matching plasma concentration level, CL_{plasma} expresses the body's overall capacity to remove a medication. A compound is said to possess high clearance if CL_{plasma}>15 ml/min/kg otherwise low clearance if CL_{plasma}: 5-15 ml/min/kg. i.e., excellent: 0-5; medium: 5-15; poor > 15. Both the compounds **1** and **2**possess medium plasma clearance.

Half-life ($T_{1/2}$): $T_{1/2}$ is expressed in hours. Drugs with ultra-short half-lives ($T_{1/2}$< 1 hour), short half-lives ($T_{1/2}$ 1-4 hours), intermediate short-lives ($T_{1/2}$ 4-6 hours), and long-lives ($T_{1/2}$> 8 hours) are all classified. In other words: excellent >8; medium: 1-8; poor <1. Since the $T_{1/2}$ of both the synthesized compounds is <1 hour, therefore they fall in the ultra-short half-life drugs category.

Toxicity: One of the main reasons for compound attrition is toxicity. According to research, preclinical (i.e., in cells or animals) attrition accounts for around 70% of all toxicity-related attrition, and these attritions are highly predictive of human toxicities. A precise toxicity prediction can increase the possibility of a product being marketed and drastically lower the compound attribution.

Human ether-a-go-go-related gene (hERG): The voltage-gated potassium channel expressed by the human ether-a-go-go-related gene plays a key role in cardiac action potential. When this hERG potassium ion channel is blocked, the QT interval lengthens and causes serious cardiotoxicity, including cardiac arrhythmia [45]. The hERG data of compounds **1** and **2** falls in the excellent category.

Drug-induced liver injury (DILI): Over the past 50 years, DILI has emerged as the most prevalent safety issue leading to drug withdrawals from the market. DILI-positive drugs include those that have been 1) taken off the market primarily due to hepatotoxicity, 2) not sold in the U.S. due to hepatotoxicity, 3) receiving black box warnings from the U.S. Food and Drug Administration due to hepatotoxicity, 4) having hepatotoxicity warnings on their labels, and 5) other drugs that have a high number (> 10) of independent clinical reports of hepatotoxicity and well-established associations with liver injury. DILI negatives are drugs that don't fit any of the aforementioned positive criteria. The data of compounds **1** and **2** falls in the category of poor DILI positive drugs.

The compound's mutagenicity is tested using the Ames test, which is employed when mutagenicity and carcinogenicity are closely related. Carcinogenic compounds have a major impact on human health because they can harm the DNA. The Ames mutagenic data indicates that both the compounds **1**&**2** are moderately Ames mutagenic while the carcinogenic data indicates that compound **1** is moderately carcinogenic while **2** is poor carcinogenic.

Skin sensitization (SS), eye irritation (EI) and ocular corrosion (EC): Assessing a compound's potential for SS, EI and EC is an essential component of risk evaluation. The SS data of both the compounds **1** and **2** falls in the range of high risk. The EC data shows that both the compounds **1** and **2** have non-sensitizer/non-irritants/non-corrosive nature while the EI data indicates that compound **1** has non-sensitizer/non-irritants/non-corrosive nature while compound **2** has high risk.

Human hepatotoxicity (H-HT): It is a crucial component of risk assessment for novel medications. The drug may be taken off the market if its effects cause liver damage and destruction, which is a serious patient safety risk. The data for both the compounds **1** and **2** falls in the range of moderate toxicity.

Drug-induced Nephrotoxicity and Neurotoxicity: Nephrotoxicity is used to adverse effect of chemicals and medications on the kidneys, frequently leading to their quick decline. Neurotoxicity is neurological (nervous system) damage due to exposure to natural or synthetic toxins such as heavy metals, pollutants, or certain medications. The data indicates that both the compounds **1** and **2** possess medium nephrotoxic as well as neurotoxic effects.

Rat Oral Acute Toxicity: It is one of the most important tasks for assessing the safety of drug candidates and is used to determine acute toxicity in mammals (such as rats or mice). The data for compounds **1** and **2** falls in the category of medium toxicity.

Respiratory toxicity: It has emerged as the primary cause of drug discontinuation among these safety concerns. Because drug-induced respiratory toxicity can have substantial morbidity and mortality and may not have clear early signs or symptoms in popular drugs, it is typically underdiagnosed. As a result, it is crucial to closely monitor and treat respiratory toxicity. The data for compound **1** comes in the category of medium respiratory toxicant while that for **2** in the category of poor toxicant.

Ototoxicity: It is inner ear damage caused by certain medications and such medications are called ototoxicants. Both the compound **1** and **2** data fall in the range of excellent.

Hematotoxicity and Genotoxicity: It is the study of how medicines, pollution from the workplace or environment, stress, exercise, and ionizing radiation can affect blood and blood-forming tissues [46]. While genotoxicity is the ability of substances to alter a cell's genetic material, causing mutations that could result in cancer. By interacting with the DNA sequence and structure, the genotoxic chemicals cause harm to the cells' genetic material. The data shows that compound **1** is excellent hematotoxic while **2** is medium. In case of genotoxicity, both **1** and **2** are poor genotoxic.

NR-AR: The nuclear hormone receptor known as the androgen receptor (AR) is essential for the development of AR-dependent prostate cancer as well as other androgen-related disorders. The data in Table 8 indicates that both the compounds **1** and **2** are highly safe means non-toxic.

Compound #	Comp. 1	Comp. 2	Optimal range
Physicochemical properties			
Molecular Weight	338.02	409.1	100 to 600
Volume & Density	308.578 & 1.095	388.7587 & 1.052	----
nHA & nHD	5.0 & 2.0	6.0 & 2.0	0 to 12 & 0 to 7
nRot & nRing	6.0 & 2.0	9.0 & 2.0	0 to 11 & 0 to 6
MaxRing	6.0	6.0	0 to 18
nHet & fChar	7.0 & 0.0	8.0 & 0.0	1 to 15 & -4 to 4
nRig	14.0	14.0	0 to 30
Flexibility	0.43	0.643	
Stereo Centers	0.0	0.0	≤ 2
TPSA	70.92	74.16	0~140
logS	-5.623	-6.019	-4 to 0.5 log mol/L
logP	4.268	4.986	0 to 3 log mol/L
$logD_{7.4}$	3.712	4.018	1 to 3 log mol/L
Adsorption			
Caco-2 Permeability	-5.227	-5.123	> -5.15
MDCK Permeability (cm/s)	-4.913×10^{-6}	-4.940×10^{-6}	Low: < 2×10^{-6}; Medium: 2-20 x 10^{-6}; High: 20×10^{-6}
PAMPA Permeability	0.813	0.010	Low < 2.0; High > 2.5
Pgp inhibitor	0.0002	0.0002	Excellent: 0-0.3; Medium: 0.3-0.7; Poor: 0.7-1; Non-inhibitor/substrate: 0
Pgp substrate	0.068	0.884	
HIA	2.38×10^{-7}	0	
F20%, F30%, F50%	0.843, 0.023, 0.869	0.415, 0.003, 0.770	Excellent: 0-0.3; Medium: 0.3-0.7; Poor: 0.7-1.0
Distribution			
PPB (%)	98.906	98.992	Excellent: ≤ 90%; otherwise: Poor
VD (L/kg)	-0.393	-0.097	Excellent: 0.04-20; otherwise: Poor
Fu	0.5895	0.588	Excellent ≥ 5%; Poor < 5%.
BBB (cm/s)	0.060	0.064	Excellent: 0-0.3; Medium: 0.3-0.7; Poor: 0.7-1.0
OATP1B1 inhibitor	0.303	0.001	
OATP1B3 inhibitor	0.983	0.196	
BCRP inhibitor	1.209×10^{-7}	1.0×10^{-5}	
MRP1 inhibitor	0.002	0.048	
BSEP inhibitor	0.293	1	
Metabolism			
CYP1A2 inhibitor & substrate	1.0 & 0.5377	1.0 & 1.0	0: Non-substrate / Non-inhibitor; 0-1: substrate / inhibitor
CYP2C19 inhibitor & substrate	1.0 & 0.0002	1.0 & 0.001	
CYP2C9 inhibitor & substrate	0.999 & 0.001	0.996 & 0.016	
CYP2D6 inhibitor & substrate	0.016 & 0.498	0.143 & 0.071	
CYP3A4 inhibitor & substrate	0.915 & 0.988	0.999 & 0.100	
CYP2B6 inhibitor & substrate	$0.477 \& 6.674 \times 10^{-9}$	$0.989 \& 2.937 \times 10^{-9}$	
CYP2C8 inhibitor	0.997	1	
HLM Stability	0.011	0.989	Poor: 0-0.3; Medium: 0.3-0.7; Excellent: 0.7-1
Excretion			
CL_{plasma}	5.743	6.205	Excellent: 0-5; Medium: 5-15; Poor> 15
$T_{1/2}$ (hour)	0.716	0.535	Excellent: >8; Medium: 1-8; Poor <1
Toxicity			
hERG Blockers	0.267	0.331	hERG blocker: 0-1 (excellent: 0-0.3; medium: 0.3-0.7; poor: 0.7-1)) or non-hERG blocker: 0
DILI	0.962	0.955	DILI +: 0-1 (excellent: 0-0.3; medium: 0.3-0.7; poor: 0.7-1); DILI -: 0
AMES Toxicity	0.35	0.546	Ames mutagenic or carcinogenic: 0 to 1 (excellent: 0-0.3; medium: 0.3-0.7; poor: 0.7-1) or non-Ames mutagenic/carcinogenic: 0
Carcinogenicity	0.555	0.755	
Skin Sensitization	0.916	0.922	Non-sensitizer/corrosive/irritant: 0; Sensitizer/corrosive/irritant: 0-1 (excellent: 0-0.3; medium: 0.3-0.7; poor: 0.7-1)
Eye Corrosion	0.0	0.001	
Eye Irritation	0.392	0.843	
Human Hepatotoxicity	0.647	0.343	
Drug-induced Nephrotoxicity	0.631	0.554	
Drug-induced Neurotoxicity	0.515	0.638	
Rat Oral Acute Toxicity	0.416	0.402	Toxic: 0-1 (excellent: 0-0.3; medium: 0.3-0.7; poor: 0.7-1); Non-Toxic: 0
Respiratory	0.545	0.968	
Ototoxicity	0.198	0.269	
Hematotoxicity	0.285	0.509	
Genotoxicity	0.978	0.997	
NA-AR	0.02	0.02	Active: 0-1 (excellent: 0-0.3; medium: 0.3-0.7; poor: 0.7-1); non- active: 0

Fig. 7: ADMET evaluation data of the compounds **1** and **2.**

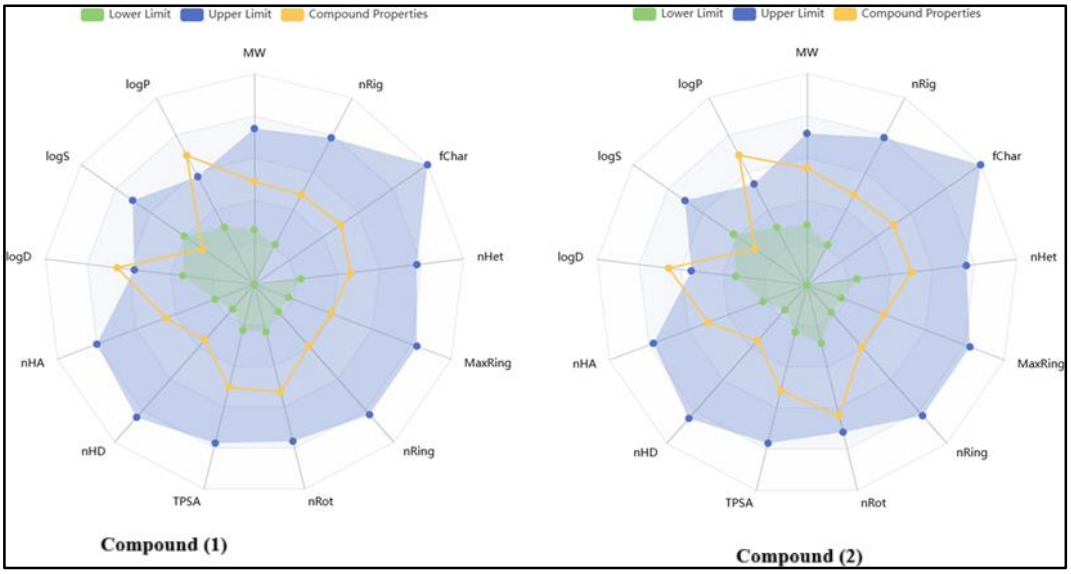

Fig. 8: Radar view of compounds**1**& **2**.

DFT results

The optimized structures of the compounds **1** and **2** are shown in Fig 9 while the bond lengths and angles are given in Tables S1-S2 of the supplementary material. Correlation of bond lengths and angles between single crystal XRD and DFT geometries is strong, indicating that DFT optimization captures the intrinsic molecular geometry reliably. For example, N-N bond length in single crystal data is 1.376 while in DFT data is 1.362Å. Generally, the gas-phase DFT geometry tends to slightly overestimate single bond lengths and underestimate multiple bond shortening.

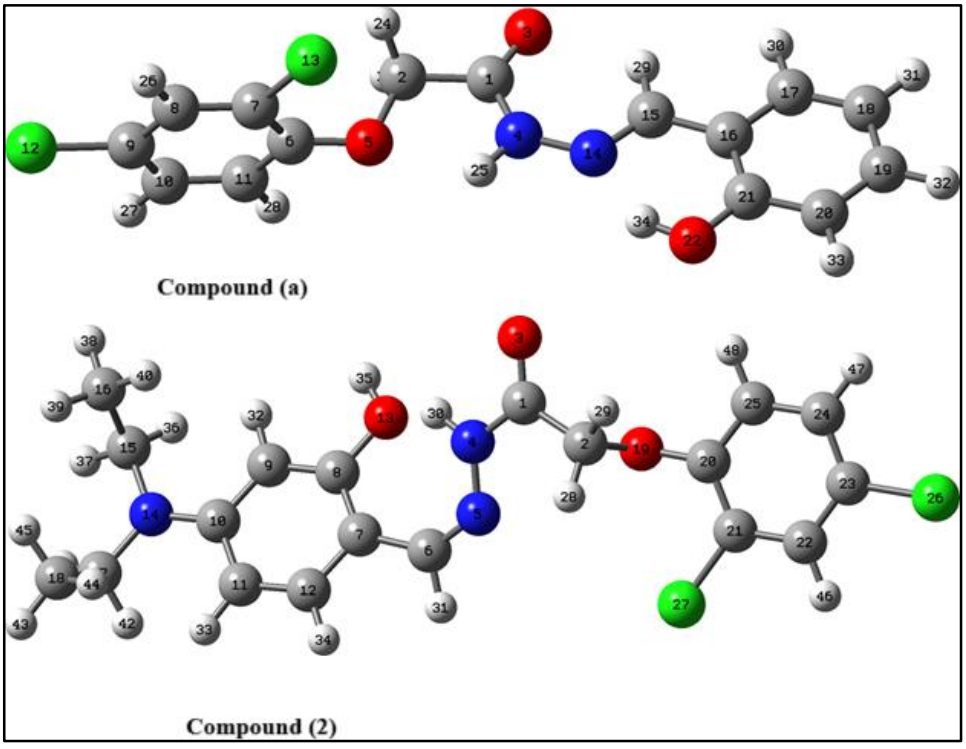

Fig. 9: DFT optimized structure of **a** and **2**.

Global reactivity parameters (GRP)

The GRP of the synthesized compounds were obtained from energies of HOMO-LUMO orbitals and energy gaps as shown in Table 5. The ionization potential (I) and electronic affinity (A), Chemical potential (μ), Global hardness (η), Electronegativity (X), Global softness (σ) and Global electrophilicity (ω) are calculated by using the following Equations (i-vii) [34, 47].

$$I = -E_{HOMO}\text{(i)} \quad A = -E_{LUMO}\text{(ii)} \quad \eta = \frac{I-A}{2}\text{(iii)}$$

$$X = \frac{I+A}{2}\text{(iv)}$$

$$\mu = \frac{E_{HOMO}+E_{LUMO}}{2}\text{(v)} \qquad \sigma = \frac{1}{2\eta}\text{(vi)} \qquad \omega = \frac{\mu^2}{2\eta}\text{(vii)}$$

Table 10 summarized the results obtained from all these equations. In general, electron affinity and ionization potential were used to elaborate on electron accepting and donating qualities. The ionization potential of compounds **1** and **2** is higher than their electron affinity values. Chemical potential value (μ) was linked to a chemical system's stability and reactivity. Reactivity and chemical potential are inversely related, although stability and reactivity are directly related. The chemical potential for compound **1** (-4.01 eV) is slightly higher than **2** (-3.44 eV). The electrophilicity (ω) is giving the information about charge transfer properties and describe the energy variations. The electrophilicity for compound **1** (3.74 eV) is slightly higher than **2** (2.75 eV). The positive charge multiplied by the distance between the charges is the electric dipole moment. Dipole moment trends for the compounds are as follows: **2** (9.65 D) > **1** (2.45 D). Since the most fascinating intermolecular interactions are typically dipole ones, the electrical dipole moment in chemistry is appropriate for characterizing a wide variety of them [48].

Frontier molecular orbital analysis

The electric and optical properties are significantly influenced by the Frontier molecular orbital (FMO) research. When determining the molecule's chemical activity, ΔE which is the energy gap between the HOMU and LUMO orbitals is important. In addition to being useful in figuring out the optical polarizability, kinetic stability, hardness, and other chemical reactivity factors, it is a key factor in the characteristics of molecular electrical transport. Gaussian software's B3LYP/6-31++G(d, p) method is used to compute the orbital energy gaps. The FMOs based on the HOMO (electron-donating ability) and the LUMO (electron-accepting ability) have the biggest impact on the compounds' stability [49]. The values of E_{HOMO} and E_{LUMO} of compounds **1** and **2** are shown in Fig 10, and ΔE is shown in Table 7. A low ΔE value indicates low kinetic stability, as it is more energy-efficient to add electrons to the LUMO and receive electrons from the HOMO easily. The energy gaps of compounds **1** and **2** are nearly comparable (slightly higher for **2**) [47].

Table-5: E_{HOMO}, E_{LUMO} and Energy gap and Global reactivity descriptors data.

Comp.	E_{HOMO} (eV)	E_{LUMO} (eV)	ΔE (eV)	E of optimized geometry (a.u)
1	-6.16	-1.86	4.30	-1834.42
2	-5.60	-1.29	4.31	-2047.01

Global reactivity descriptors								
Comp.	I (eV)	A (eV)	μ (eV)	η (eV)	X (eV)	σ (eV)	ω (eV)	D.M (Debye)
1	6.16	1.86	-4.01	2.15	4.01	0.23	3.74	2.45
2	5.60	1.29	-3.44	2.16	3.44	0.23	2.75	9.65

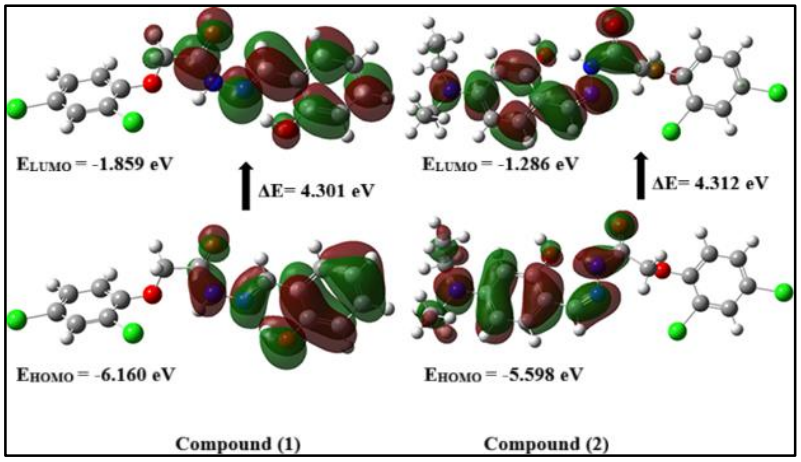

Fig. 10: Frontier molecular orbitals (HOMO and LUMO) in the gas phase, and ΔE for 1&2.

Molecular electrostatic potential (MEP)

Fig 11 showed the molecular electrostatic potential utilizing B3LYP/6-31G (d, p), as well as the contour and surface map for compounds **1** and **2**. Red areas indicate the nucleophilic zone, blue areas show the positive electrostatic potential, yellow areas show the slightly rich electron, and green areas show the neutral potential. The hydroxyl group connected to the benzene ring, the carbonyl oxygen that experiences electrophilic reactivity, and the phenolic oxygen are all highly negatively charged for both compounds. The blue patches represent the regions of strongest interaction and is usually filled with H-atoms. The MEP, which displays an isosurface with red lines denoting atoms having strong e⁻withdrawing potentials, such as the O atoms in the carbonyl, hydroxyl, and phenolic units of both compounds, supports the MEP results.

Intermolecular interactions and energies by HSA

The d_{norm} surface, which is represented in a red-blue-white color scheme, is used to characterize interactions between molecules that are adjacent to one another. Intermolecular interactions with distances less than, equal to, and larger than the van der Wall radii are indicated by red, white, and blue color spots, respectively [50]. The brief interactions found in compounds **a** and **2** are represented by the red spots on the Hirshfeld surface (d_{norm}) (Fig 10). The distinctive packing and stacking modes as well as the manner in which nearby molecules interact with one another are identified using the shape indexes. Total volume (244.16 & 487.04 $Å^3$), area (244.23 & 449.11 $Å^2$), globularity (0.77 & 0.67), and asphericity (0.28 & 0.52) are the quantitative measurements of the Hirshfeld surface for compounds **a** and **2**. The molecule surfaces are more organized when the globularity value is less than 1.0. An electrostatic potential map projected on the Hirshfeld surface is used to identify the electrophilic and nucleophilic regions. The oxygen atoms are good electron acceptors, as shown by the red areas around them (Fig 12) [51]. The definite input to the total HS area is displayed in 2D-fingureprint graphs. Fig 13A & B display the chosen decomposed fingerprint plots for compounds **a** and **2**. The primary inputs come from H-H, O-H, and Cl-H [51].

The interaction energy between the molecules was calculated using the Mackenzie et al. suggested approach [37]. The total interaction energy was determined by encircling the chosen molecule with a molecular cluster of radius 3.8 Å. In the energy framework calculations, symmetry operations were used to calculate the cluster of molecules' wave functions and electron densities. The pairwise intermolecular interaction energies are shown in the energy framework as cylinders with radii that correspond to the strength of the molecular connection. Fig 14A shows the pairwise interaction energy between molecules **a** and **2** within the crystals. Electrostatic or coulomb energy (E_ele), polarization energy (E_pol), dispersion energy (E_dis), and repulsion energy (E_rep) comprise the total interaction energy. Fig 13B shows the overall energy for both molecules as well as each component's energy. The construction of the 3D topological frame of the principal interactions using the energies indicated above is shown in Fig 14B. Relative contact energy strengths are represented by the radii of cylinders that connect the molecules' centroids [50, 52]. Dispersion and repulsion energies are the predominant components, according to the data in Fig 14B.

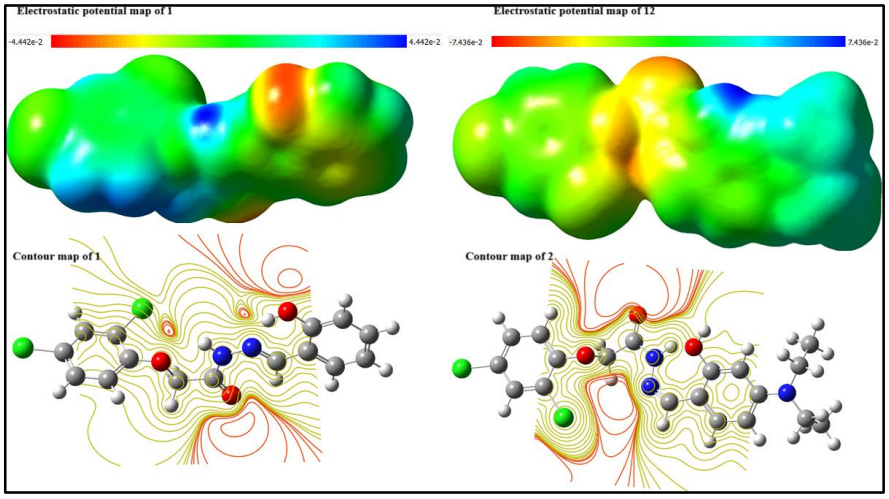

Fig. 11: Electrostatic potential and contour maps for 1 & 2 at isosurface: 0.02 a.u and isodensity: 0.0004 a.u.

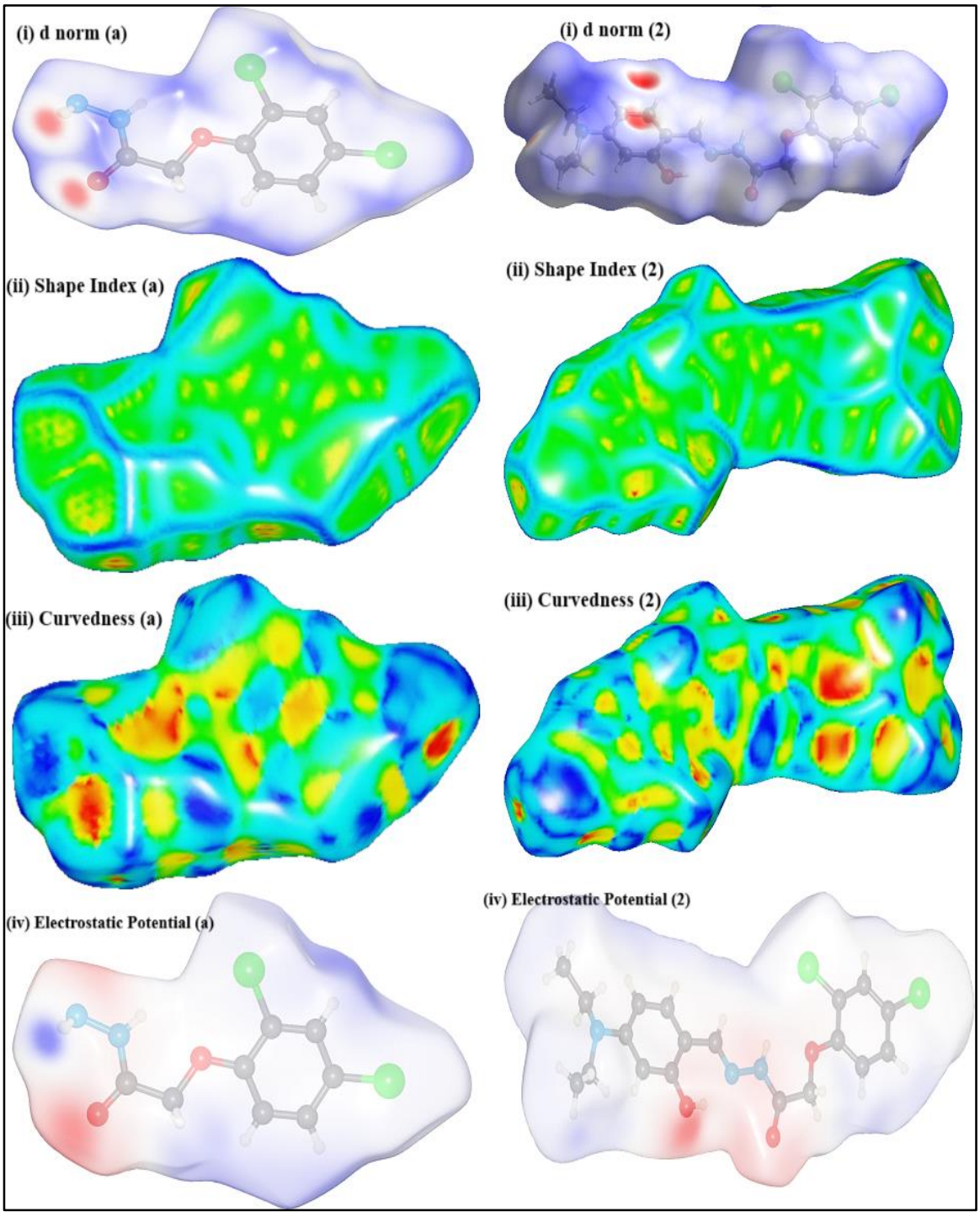

Fig. 12: HS mapped for (i) d_{norm} (ii) shaped index (iii) curvedness (iv) electrostatic potential.

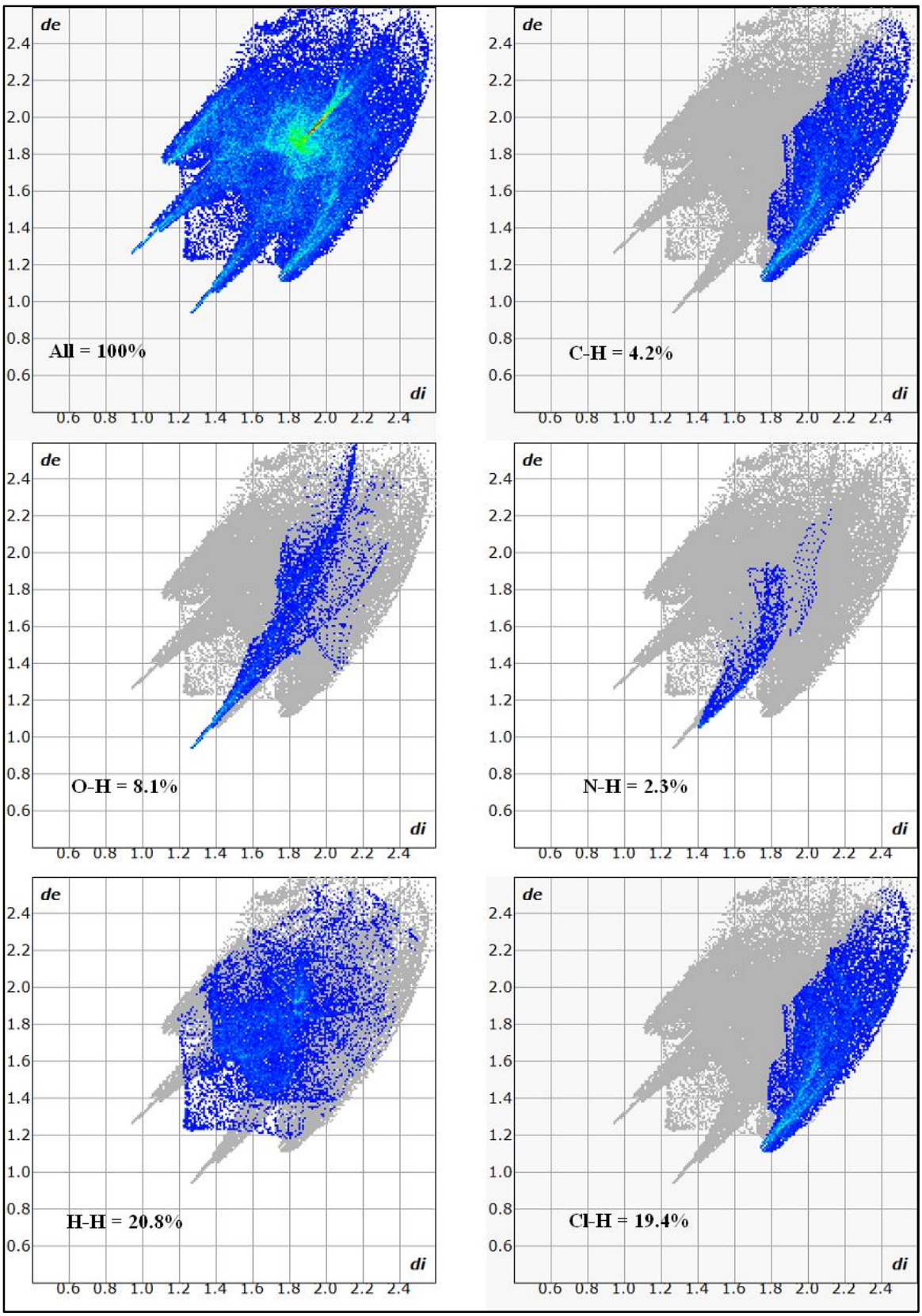

Fig. 13A: 2D-fingerprint plots showing percent contribution of total Hirshfeld surface of **a**.

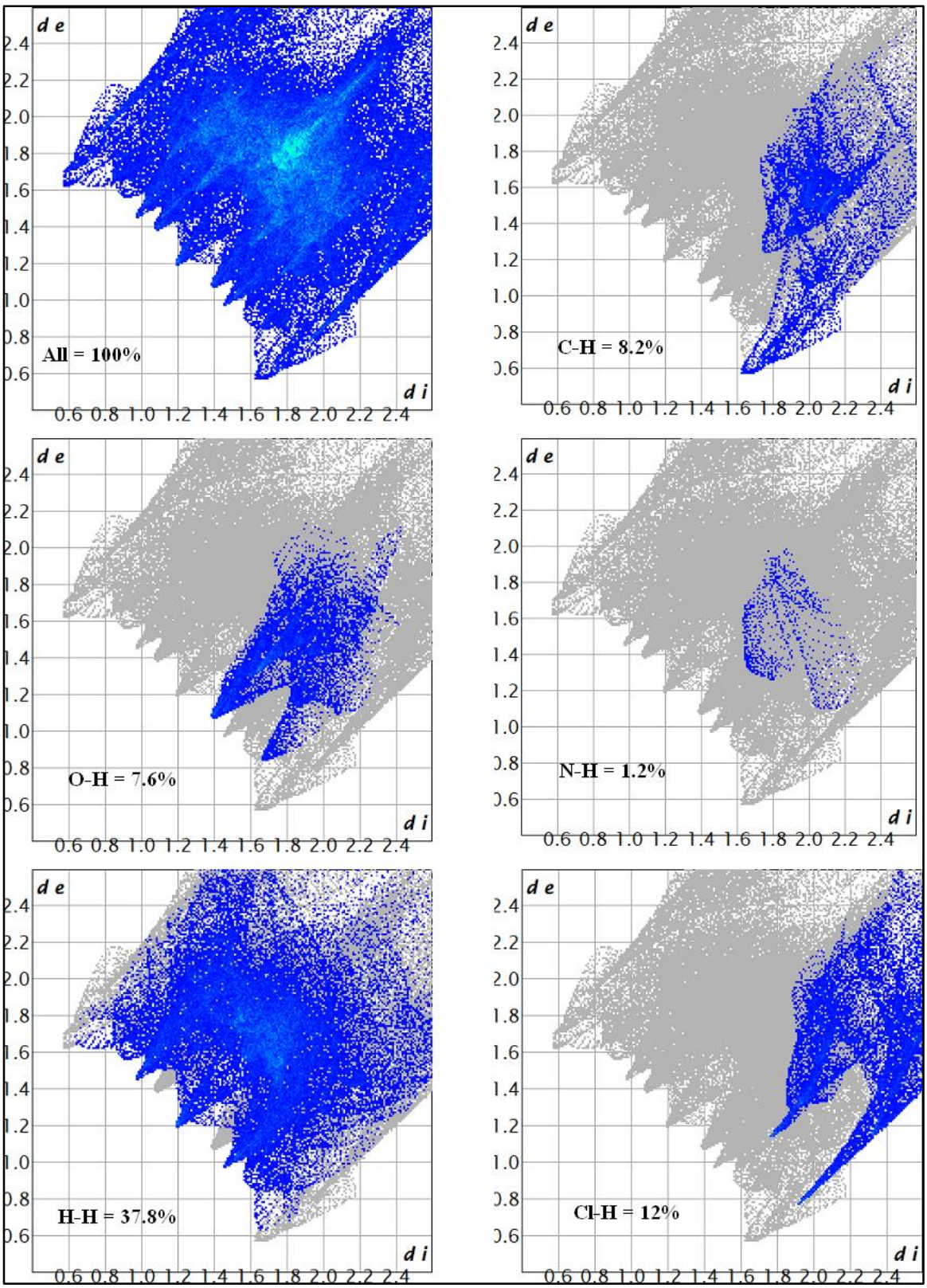

Fig. 13B: 2D-fingerprint plots showing percent contribution of total Hirshfeld surface of **2**.

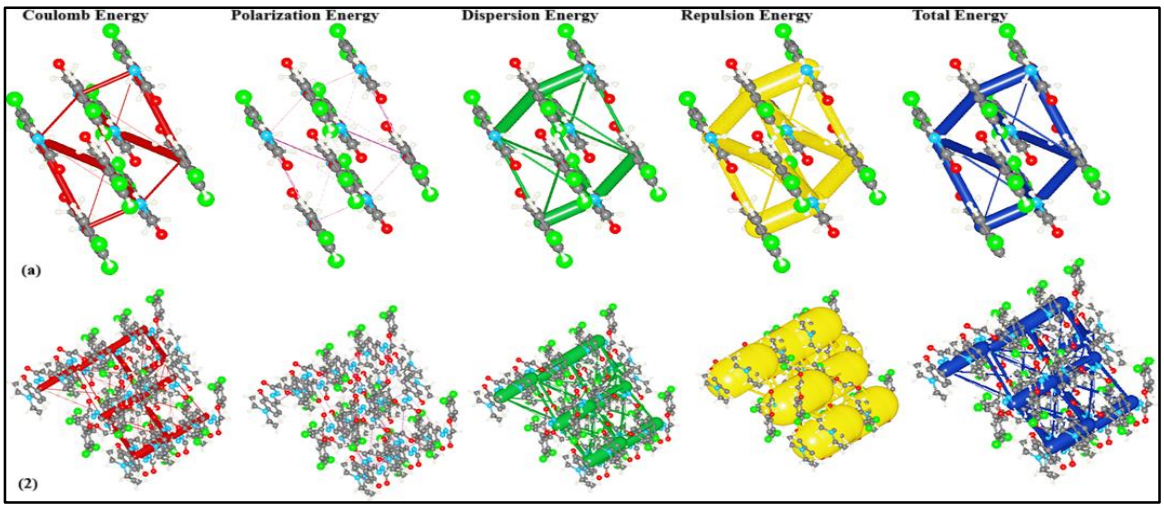

Fig. 14A: Energy framework of compounds a & 2 showing $E_{\_ele}$, $E_{\_pol}$, $E_{\_dis}$, $E_{\_rep}$, and $E_{\_tot}$. The details of interaction of interaction with color-coded, symmetry operation and distances between molecular centroids (R) in Å.

a

N	Symop	R	Electron Density	E_ele	E_pol	E_dis	E_rep	E_tot
1	-x, -y, -z	9.14	B3LYP/6-31G(d,p)	-32.0	-4.8	-20.6	34.1	-34.2
1	-x, -y, -z	7.84	B3LYP/6-31G(d,p)	-6.6	-0.8	-16.2	22.7	-7.6
1	-x, -y, -z	4.35	B3LYP/6-31G(d,p)	-6.4	-1.1	-47.6	22.8	-35.0
1	-x, -y, -z	3.85	B3LYP/6-31G(d,p)	-17.5	-2.3	-63.1	40.7	-50.0
2	x, y, z	7.34	B3LYP/6-31G(d,p)	-1.5	-0.6	-8.1	4.6	-6.3
1	-x, -y, -z	10.35	B3LYP/6-31G(d,p)	-7.2	-0.6	-9.2	15.8	-6.3
1	-x, -y, -z	11.46	B3LYP/6-31G(d,p)	-36.8	-7.1	-10.8	34.7	-32.1
2	x, y, z	8.53	B3LYP/6-31G(d,p)	2.2	-0.5	-10.6	4.6	-4.4
1	-x, -y, -z	7.90	B3LYP/6-31G(d,p)	-27.7	-7.4	-15.2	19.6	-35.9

2

N	Symop	R	Electron Density	E_ele	E_pol	E_dis	E_rep	E_tot
1	-x, -y, -z	9.54	B3LYP/6-31G(d,p)	-34.4	-9.9	-20.4	25.5	-45.7
2	-x+1/2, y+1/2, -z+1/2	10.14	B3LYP/6-31G(d,p)	0.2	-0.2	-5.0	0.7	-3.8
2	-x+1/2, y+1/2, -z+1/2	11.63	B3LYP/6-31G(d,p)	-4.3	-2.4	-23.0	9.7	-20.4
2	x, y, z	4.98	B3LYP/6-31G(d,p)	-45.8	-5.7	-123.6	141.8	-72.7
1	-x, -y, -z	12.58	B3LYP/6-31G(d,p)	-3.4	-0.3	-16.5	13.1	-10.1
2	x+1/2, -y+1/2, z+1/2	16.70	B3LYP/6-31G(d,p)	0.6	-0.1	-4.3	0.2	-3.1
2	-x+1/2, y+1/2, -z+1/2	14.75	B3LYP/6-31G(d,p)	-3.4	-2.5	-19.2	13.7	-13.8
1	-x, -y, -z	11.66	B3LYP/6-31G(d,p)	0.4	-4.2	-16.4	7.1	-12.5

Fig. 14B: Interaction energies (kJ/mol), R is the distance between molecular centeroids in Å and N is the number of molecular pairs involved.

Conclusion

The synthesized Schiff bases **1** & **2** were confirmed by the presence of CH=N confirmative peak in the spectra of FTIR and NMR. The antibacterial activity data shows the significant activity for **1** & **2** against the tested bacterial strains. Furthermore, in silico ADMET properties were predicted and their likelihood was noted. The quantum chemical calculations were performed, including HOMO, LUMO, and energy band gap. Finally, molecular docking study was performed using double strand DNA receptor with PDB# 1BNA. The results of in vitro DNA interaction fully match with those of the molecular docking. The binding constant of compound **2** is higher than that of **1** and same was observed in docking study in which the docking score of **2** (-7.59) is higher than that of **1** (-7.39). Compound **1** interact with DT A8 nucleotide of DNA in H-acceptor fashion while compound **2** interacts with DG A10 nucleotide in H-donor fashion via NH and CH_2 groups. Both the techniques confirm the intercalative binding mode of interaction between the compounds and SS-DNA. All the physicochemical properties of the synthesis compounds **1** and **2** follow the drug recommended range except in case of logS and $logD_{7.4}$ for compounds **1** and **2** which show small deviation from the upper limit of drug recommended range. Both the compounds **1** and **2** obey the Lipinski, Ghose and Veber rules of drug. Compounds **1** and **2** possess medium plasma clearance and $T_{1/2}$ of ultra-short half-life drugs. They are non-toxic for NR-AR. The smaller ΔE values for both the compounds show that they have good chemical reactivity. These compounds possess good potential for further development due to their notable DNA binding and antibacterial activities. Future studies may focus on detailed in vitro and in vivo biological evaluation and exploration of their mechanism of action. Such investigation might facilitate the development of these compounds as potential therapeutic agents and broaden their applicability in medicinal chemistry.

References

1. L. Lv, T. Zheng, L. Tang, Z. Wang and W. Liu, Recent advances of Schiff base metal complexes as potential anticancer agents, *Coord. Chem. Rev.*, **525**, 216327 (2025).
2. M. Sirajuddin, S. Ali, A. Haider, N. A. Shah, A. Shah and M. R. Khan, Synthesis, characterization, biological screenings and interaction with calf thymus DNA as well as electrochemical studies of adducts formed by azomethine [2-((3, 5-dimethylphenylimino) methyl) phenol] and organotin (IV) chlorides, *Polyhedron*, **40**, 19 (2012).
3. M. Sirajuddin, S. Ali, F. A. Shah, M. Ahmad and M. N. Tahir, Potential bioactive Vanillin–Schiff base di-and tri-organotin (IV) complexes of 4-((3, 5-dimethylphenylimino) methyl)-2-methoxyphenol: synthesis, characterization and biological screenings, *J. Iran. Chem. Soc.*, **11**, 297 (2014).
4. G. Matela, Schiff bases and complexes: a review on anti-cancer activity, *Anti-Cancer Agents Med. Chem.*, **20**, 1908 (2020).
5. E. Raczuk, B. Dmochowska, J. Samaszko-Fiertek and J. Madaj, Different Schiff bases—structure, importance and classification, *Molecules*, **27**, 787 (2022).
6. S. Tighadouini, S. Radi, L. Toupet, M. Sirajuddin, T. B. Hadda, M. Akkurt, I. Warad, Y. N. Mabkhot and S. Ali, Origin and switch of different colors: Thermo-isomerism and crystal structure of (1E, 2E)-bis [1-(4-nitrophenyl) ethylidene] hydrazine, *J. Chem. Sci.*, **127**, 2211 (2015).
7. Ş. Atalay, Synthesis, spectroscopic characterizations, comparison of experimental, theoretical results, and molecular docking of novel hydrazone Schiff base compound N'-(4-hydroxy-3, 5-dimethoxybenzylidene)-1-(2-methoxyphenyl)-5-methyl-1H-pyrazole-4-carbohydrazide, *J. Iran. Chem. Soc.*, 1 (2025).
8. C. Cheng, J. Sun, C. Wang, Y. Zhang, S. Wei, F. Jiang and Y. Wu, Protonated N′-benzyl-N′-prolyl proline hydrazide as highly enantioselective catalyst for direct asymmetric aldol reaction, *Chem. Commun.*, 215 (2006).
9. X. Xiong, Y. Jiang and D. Ma, Assembly of N, N-disubstituted hydrazines and 1-aryl-1 H-indazoles via copper-catalyzed coupling reactions, *Org. Lett.*, **14**, 2552 (2012).
10. J.-G. Roveda, C. Clavette, A. D. Hunt, S. I. Gorelsky, C. J. Whipp and A. M. Beauchemin, Hydrazides as tunable reagents for alkene hydroamination and aminocarbonylation, *J. Am. Chem. Soc.*, **131**, 8740 (2009).
11. T. T. Wang, F. L. Yang and S. K. Tian, Copper-Catalyzed Sulfenylation of Boronic Acids with Sulfonyl Hydrazides, *Adv. Synth. Catal.*, **357**, 928 (2015).
12. P. E. Marinova and K. D. Tamahkyarova, Synthesis, investigation, biological evaluation, and application of coordination compounds with schiff base—a review, *Compounds*, **5**, 14 (2025).
13. E. Uddin, M. N. Sardar, M. S. Reza, M. S. Hasan, M. T. Talukder, M. M. Hoque, P. Paul, M. S. Khatun, M. F. Hossen and M. A. Asraf, Emerging pharmaceutically active drugs: synthesis and pharmacology of Schiff base ligands with their

metal complexes, *Discover Chemistry*, **2**, 153 (2025).
14. M. S. Al-Ajely and A. N. Yaseen, Synthesis and characterization of some new hydrazides and their derivatives, *Ibn al-Haitham J. Pure Appl. Sci.*, **28**, 103 (2017).
15. J. Devi, B. Kumar and B. Taxak, Recent Advancements of Organotin (IV) Complexes Derived from Hydrazone and Thiosemicarbazone Ligands as Potential Anticancer Agents, *Inorg. Chem. Commun.*, 109208 (2022).
16. Zainab, F. Khan, A. Alam, N. U. Rehman, S. Ullah, A. A. Elhenawy, M. Ali, W. U. Islam, A. Khan, A. Al-Harrasi and M. Ahmad, Synthesis, anticancer, α-glucosidase inhibition, molecular docking and dynamics studies of hydrazone-Schiff bases bearing polyhydroquinoline scaffold: In vitro and in silico approaches, *J. Mol. Struct.*, **1321**, 139699 (2025).
17. S. Ahmad, M. Khan, M. I. A. Shah, M. Ali, A. Alam, M. Riaz and K. M. Khan, Synthetic transformation of 2-{2-fluoro [1, 1′-biphenyl]-4-yl} propanoic acid into hydrazide–hydrazone derivatives: in vitro urease inhibition and in silico study, *ACS Omega*, **7**, 45077 (2022).
18. R. Ahmad, A. Alam, M. Khan, T. Ali, A. A. Elhenawy and M. Ahmad, Antioxidant activity, molecular docking and quantum studies of new bis-schiff bases based on benzyl phenyl ketone moiety, *ChemistrySelect*, **8**, e202302338 (2023).
19. M. Khan, M. A. Hanif, K. Rehman, M. Arif, H. Nazir, S. W. Khan, A. Kangal, R. Abid, D. A. Al Farraj and M. S. Elshikh, Molecular docking and in vitro antibacterial activity of chiral phthalimide on ESBL producing gram negative bacteria, *Pak. J. Pharm. Sci.*, **36**, (2023).
20. K. M. Khan, M. Khan, M. Ali, M. Taha, S. Rasheed, S. Perveen and M. I. Choudhary, Synthesis of bis-Schiff bases of isatins and their antiglycation activity, *Bioorg. Med. Chem.*, **17**, 7795 (2009).
21. W. U. Islam, A. Khan, F. Khan, S. Ullah, M. Waqas, H. Khan, M. Khan, S. M. Rahman, S. Ali and A. Mateen, Synthesis of novel hydrazide Schiff bases with anti-diabetic and anti-hyperlipidemic effects: in-vitro, in-vivo and in-silico approaches, *J. Biomol. Struct. Dyn.*, 1 (2024).
22. S. Murtaza, M. S. Akhtar, F. Kanwal, A. Abbas, S. Ashiq and S. Shamim, Synthesis and biological evaluation of schiff bases of 4-aminophenazone as an anti-inflammatory, analgesic and antipyretic agent, *J. Saudi Chem. Soc.*, **21**, S359 (2017).
23. A. Shakoor, A. Alam, F. Jan, M. Khan, M. Ali, S. Ullah, A. Khan, A. F. AlAsmari, F. Alasmari and A. Al-Ghafri, Novel benzimidazole derivatives as effective inhibitors of prolyl oligopeptidase: synthesis, in vitro and in silico analysis, *Future Med. Chem.*, **16**, 43 (2024).
24. M. Khan, F. Alam, M. Ateeq, A. Wadood, M. Ali, S. Shah, A. Alam, M. Yousaf and A. Ali, 4-Bromobenzohydrzide Derivatives as Potent α-amylase Enzyme Inhibitors; Synthesis, in Vitro and in Silico Studies, (2022).
25. F. Pammolli, L. Magazzini and M. Riccaboni, The productivity crisis in pharmaceutical R&D, *Nat. Rev. Drug Discovery*, **10**, 428 (2011).
26. L. Fu, S. Shi, J. Yi, N. Wang, Y. He, Z. Wu, J. Peng, Y. Deng, W. Wang and C. Wu, ADMETlab 3.0: an updated comprehensive online ADMET prediction platform enhanced with broader coverage, improved performance, API functionality and decision support, *Nucleic Acids Res.*, **52**, W422 (2024).
27. H. Dowden and J. Munro, Trends in clinical success rates and therapeutic focus, *Nat Rev Drug Discov*, **18**, 495 (2019).
28. T. Takebe, R. Imai and S. Ono, The current status of drug discovery and development as originated in United States academia: the influence of industrial and academic collaboration on drug discovery and development, *Clin. Transl. Sci.*, **11**, 597 (2018).
29. R. K. Harrison, Phase II and phase III failures: 2013–2015, *Nat. Rev. Drug Discovery*, **15**, 817 (2016).
30. N. Naz, M. Sirajuddin, A. Haider, S. M. Abbas, S. Ali, A. Wadood, M. Ghufran, G. Rehman and B. Mirza, Synthesis, characterization, biological screenings and molecular docking study of Organotin (IV) derivatives of 2, 4-dichlorophenoxyacetic acid, *J. Mol. Struct.*, **1179**, 662 (2019).
31. M. Sirajuddin, S. Ali, V. McKee, S. Z. Khan and K. Malook, Synthesis, spectroscopic characterization, crystal structure, DNA interaction study and in vitro biological screenings of 4-(5-chloro-2-hydroxyphenylamino)-4-oxobut-2-enoic acid, *Spectrochim. Acta, Part A*, **134**, 244 (2015).
32. S. Murtaza, S. Shamim, N. Kousar, M. N. Tahir, M. Sirajuddin and U. A. Rana, Synthesis, biological investigation, calf thymus DNA binding and docking studies of the sulfonyl hydrazides and their derivatives, *J. Mol. Struct.*, **1107**, 99 (2016).
33. B. Hanifa, N. Bibi, M. Sirajuddin, E. R. T. Tiekink, M. Kubicki, I. Khan, A. Bari, A. Wadood and S. Shams, Synthesis, spectral characterisation, biocidal investigation, in-silico and molecular docking studies of 4-[(2-chloro-4-methylphenyl) carbamoyl] butanoic acid derived triorganotin (IV) compounds, *J. Biomol. Struct. Dyn.*, 1 (2023).
34. R. Khan, S. Rani, M. Tariq, F. Rasool, A. Hussain, K. Mahmood, H. M. Asif, M. Usman and M.

Sirajuddin, Experimental and theoretical studies on new organotin (IV) complexes with oxygen donor ligand: DNA binding, molecular docking and antimicrobial activity, *J. Chem. Sci.,* **135**, 90 (2023).
35. D. Jayatilaka, S. K. Wolff, D. J. Grimwood, J. J. McKinnon and M. A. Spackman, CrystalExplorer: a tool for displaying Hirshfeld surfaces and visualising intermolecular interactions in molecular crystals, *Acta Crystallogr., Sect. A*, **62**, s90 (2006).
36. J. J. McKinnon, D. Jayatilaka and M. A. Spackman, Towards quantitative analysis of intermolecular interactions with Hirshfeld surfaces, *Chem. Commun.*, 3814 (2007).
37. C. F. Mackenzie, P. R. Spackman, D. Jayatilaka and M. A. Spackman, CrystalExplorer model energies and energy frameworks: extension to metal coordination compounds, organic salts, solvates and open-shell systems, *IUCrJ*, **4**, 575 (2017).
38. M. Tahir, M. Sirajuddin, A. Haider, S. Ali, A. Nadhman and C. Rizzoli, Synthesis, spectroscopic characterization, crystal structure, interaction with DNA, CTAB as well as evaluation of biological potency, docking and molecular dynamics studies of N-(3, 4, 5-trimethoxybenzylidene)-2, 3-dimethylbenzenamine, *J. Mol. Struct.,* **1178**, 29 (2019).
39. A. Munir, M. Sirajuddin, M. Zubair, A. Haider, S. Tirmizi, S. Ali, H. Khan, K. Ullah and I. Aziz, Synthesis, spectroscopic characterization, and biological screening of levofloxacin based organotin (IV) derivatives, *Russ. J. Gen. Chem.*, **87**, 2380 (2017).
40. Y.-J. Duan, L. Fu, X.-C. Zhang, T.-Z. Long, Y.-H. He, Z.-Q. Liu, A.-P. Lu, Y.-F. Deng, C.-Y. Hsieh and T.-J. Hou, Improved GNNs for log D 7.4 prediction by transferring knowledge from low-fidelity data, *J. Chem. Inf. Model.*, **63**, 2345 (2023).
41. A. S. Hassan, N. M. Morsy, W. M. Aboulthana and A. Ragab, Exploring novel derivatives of isatin-based Schiff bases as multi-target agents: design, synthesis, in vitro biological evaluation, and in silico ADMET analysis with molecular modeling simulations, *RSC Adv.*, **13**, 9281 (2023).
42. A. K. Ghose, V. N. Viswanadhan and J. J. Wendoloski, A knowledge-based approach in designing combinatorial or medicinal chemistry libraries for drug discovery. 1. A qualitative and quantitative characterization of known drug databases, *J. Comb. Chem.*, **1**, 55 (1999).
43. D. F. Veber, S. R. Johnson, H.-Y. Cheng, B. R. Smith, K. W. Ward and K. D. Kopple, Molecular properties that influence the oral bioavailability of drug candidates, *J. Med. Chem.*, **45**, 2615 (2002).
44. C. A. Lipinski, F. Lombardo, B. W. Dominy and P. J. Feeney, Experimental and computational approaches to estimate solubility and permeability in drug discovery and development settings, *Adv. Drug Delivery Rev.*, **64**, 4 (2012).
45. M. Shan, C. Jiang, J. Chen, L.-P. Qin, J.-J. Qin and G. Cheng, Predicting hERG channel blockers with directed message passing neural networks, *RSC Adv.*, **12**, 3423 (2022).
46. *Hematotoxicity*, *Dictionary of Toxicology*, Springer Nature Singapore, Singapore, 2024, pp. 453.
47. B. Saranya and M. Gowri, Synthesis, Characterization, DFT study and Molecular Docking of (Z)-4-((2-hydroxy-3-methoxy benzylidene) amino)-1, 5-dimethyl-2-phenyl-1, 2-dihydro-3H-pyrazol-3-one and its Metal Complexes, *J. Mol. Struct.,* **1250**, 131674 (2022).
48. M. Salihović, M. Pazalja, S. Š. Halilović, E. Veljović, I. Mahmutović-Dizdarević, S. Roca, I. Novaković and S. Trifunović, Synthesis, characterization, antimicrobial activity and DFT study of some novel Schiff bases, *J. Mol. Struct.*, **1241**, 130670 (2021).
49. H. A. Khamees, F. H. Al-Ostoot, O. Pinto, T. Gopichand and M. Shivappaa, In-silico docking, synthesis, structure analysis, DFT calculations and energy frameworks of metal complexes to regress angiogenesis activity, *J. Mol. Struct.*, **1253**, 132272 (2022).
50. K. Chandini, M. N. Khadri, N. Amoghavarsha, M. Sridhar and S. A. Khanum, Synthesis, crystal structure, Hirshfeld surface analysis, energy frameworks and computational studies of Schiff base derivative, *Heliyon*, **8**, (2022).
51. M. A. Spackman and D. Jayatilaka, Hirshfeld surface analysis, *CrystEngComm*, **11**, 19 (2009).
52. T. Yeşilkaynak, F. N. Özkömeç, M. Çeşme, R. E. Demirdöğen, C. V. Sezer, H. M. Kutlu and F. M. Emen, Novel thiourea derivative compounds: Thermal behavior, biological evaluation, Hirshfeld surfaces and frontier orbitals analyses, in silico ADMET profiling and molecular docking studies, *J. Mol. Struct.*, **1280**, 135086 (2023).